

Distribution Agreement

In presenting this thesis as a partial fulfillment of the requirements for a degree from Emory University, I hereby grant to Emory University and its agents the non-exclusive license to archive, make accessible, and display my thesis in whole or in part in all forms of media, now or hereafter now, including display on the World Wide Web. I understand that I may select some access restrictions as part of the online submission of this thesis. I retain all ownership rights to the copyright of the thesis. I also retain the right to use in future works (such as articles or books) all or part of this thesis.

Zoe Hughes

April 10, 2024

Investigating Lithium Enrichment in Infrared Excess K-G Giants

by

Zoe Hughes

Alissa Sue Bans, Ph.D.

Adviser

Department of Chemistry

Alissa Sue Bans, Ph.D.

Adviser

Raphael Ribeiro, Ph.D.

Committee Member

Erin Bonning, Ph.D.

Committee Member

Merida Batiste, Ph.D.

Committee Member

2024

Investigating Lithium Enrichment in Infrared Excess K-G Giants

By

Zoe Hughes

Alissa Sue Bans, Ph.D.

Adviser

An abstract of
a thesis submitted to the Faculty of Emory College of Arts and Sciences
of Emory University in partial fulfillment
of the requirements of the degree of
Bachelor of Science with Honors

Department of Chemistry

2024

Abstract

Investigating Lithium Enrichment in Infrared Excess in K-G Giants

By Zoe Hughes

The observance of anomalously high lithium abundances in K-G type giant stars challenges conventional models of stellar evolution, prompting a deeper investigation into the underlying processes responsible for this phenomenon. In this study, we present a comprehensive analysis of a sample of K-G giants exhibiting peculiar lithium enrichments, leveraging optical spectra obtained from the FAST and REOSC spectrographs. Through examination of equivalent widths of the lithium absorption line at 6707.8 Angstroms, we quantify lithium abundances and explore potential correlations with other stellar parameters like infrared excess, metallicity, and projected rotational velocity. Our analysis encompasses a diverse range of evolutionary stages, including giants in the HB red clump, RGB helium flash tip/AGB, subgiant, and RGB luminosity bump phases. This study represents a significant step towards unraveling the complex interplay between stellar evolution, nucleosynthesis processes, and lithium enrichment in K-G giant stars, paving the way for a deeper understanding of the stellar evolution of giants and the short-lived mechanisms of lithium enrichment they may involve.

Investigating Lithium Enrichment in Infrared Excess K-G Giants

By

Zoe Hughes

Alissa Sue Bans, Ph.D.

Adviser

A thesis submitted to the Faculty of Emory College of Arts and Sciences
of Emory University in partial fulfillment
of the requirements of the degree of
Bachelor of Science with Honors

Department of Chemistry

2024

Acknowledgements

I would like to first acknowledge my thesis advisor Dr. Alissa Bans for her endless support and assistance developing this project from the very start over the last year. Thank you for finding a way for me to delve into astronomy and astrophysics research using my chemistry background, for helping me navigate unfamiliar territory and software with patience and confidence, and most importantly for taking the time to be a wonderful mentor and advisor. Your belief in me, in helping me explore something I am passionate about, has helped open many possible doors and opportunities for the future that I am so excited to explore.

I would also like to extend my gratitude to Dr. Erin Bonning and Dr. Merida Batiste. My first steps venturing outside the world of chemistry and into that of physics and astrophysics was with both of your guidance. Thank you both for your support and kindness, for teaching with such kindness and passion that has inspired me to see how I can take my chemistry and physics foundation and apply it to further studying astrophysical phenomena. It was in your classes, your discussions of research and the evolution of galaxies and the universe that allowed my passion for space to bloom, leading me to where I am now; I could not be more grateful.

I extend my thanks and gratitude to Dr. Ribeiro, for introducing me to the most fascinating aspect of chemistry in my eyes - physical chemistry. It was you, who so eloquently described the narrow boundaries between chemistry and physics as nothing more than “lines humans drew,” because in fact, everything is connected in describing the universe and the laws of nature. Quantifying our existence, the existence and behavior of matter and energy, is where physics, chemistry, astrophysics, quantum mechanics - where all these fields come together harmoniously. I would not have pursued this research or developed my passion for physical chemistry without your course and subsequent advising and guidance, for which I am very grateful.

To James Kelvin, I extend my thanks and gratitude in supporting my transition from researching the applications of chemistry in drug development to astrophysical and astrochemical spectral trends. I was fascinated by your graduate dissertation research, by the applications of chemistry to cancer treatment drug development, particularly with a nanoparticle drug delivery system. Yet your support upon my transition out of the lab, your suggestions of MD/PhD programs catered to space and medical research, and your general enthusiasm and validation in my research interests and journey have left a lasting impact on me. Thank you for urging me to follow my passions, to find my own spaces to grow and learn in.

Finally, I want to thank my family. To my parents, who have infinitely supported me and my journey across the country to pursue chemistry and its many research applications. Your endless love and support, even as I navigate where I want to continue my research exploration, whether that includes graduate school or medical school, means the world to me. Especially my little sister, Phoebe, who makes me feel like I can accomplish and pursue anything I put my mind to - I would not be where I am today without you.

Contents

CHAPTER 1	1
INTRODUCTION	1
1.1 EVALUATING CURRENT MODELS OF STELLAR EVOLUTION	1
1.1.1 <i>General Processes of Red Giant Evolution by Stellar Mass Profile</i>	3
1.1.2 <i>Lithium Enrichment in Evolved Intermediate-Mass Giants Contradict</i>	5
<i>Current Models of Stellar Evolution</i>	5
1.2 IDENTIFICATION OF LITHIUM ENRICHED DISK DETECTIVE IR EXCESS OBJECTS	6
1.3 EXISTING HYPOTHESES FOR ORIGINS OF LITHIUM ENRICHMENT IN GIANTS	8
1.3.1 <i>In situ Lithium Enrichment Mechanisms</i>	8
1.3.2 <i>Auto-enrichment Lithium Generating Mechanisms</i>	11
1.4 CONSTRUCTING A NOVEL APPROACH TO THE LITHIUM ENRICHMENT DISCOURSE	15
CHAPTER 2: METHODS	17
2.1 CONSTRAINING STELLAR PARAMETERS OF OUR SET OF IR EXCESS K-G GIANTS	17
2.1.1 <i>Obtaining Stellar Effective Temperature via HR Diagram</i>	17
2.1.2 <i>Estimating Surface Gravity via Absolute Magnitude and</i>	20
<i>Stellar Evolutionary Tracks</i>	20
2.2 ACCOUNTING FOR RADIAL VELOCITY	22
2.3 DERIVING LITHIUM ABUNDANCE.....	25
2.3.1 <i>Spectral Line Equivalent Width Evaluation</i>	25
2.3.2 <i>Lithium Abundance Evaluation</i>	27
2.4 DERIVING METALLICITY	30
2.4.1 <i>Generating Synthetic Spectra Using pyMOOG</i>	31
2.4.2 <i>Developing the Chi-Squared Minimization Scheme</i>	32
2.5 DERIVING PROJECTED ROTATIONAL VELOCITY VIA IRON LINES'	34
FULL-WIDTH HALF MAX VALUES	34
2.5.1 <i>Determining Significant Iron Lines</i>	35
2.5.2 <i>FWHM and Project Rotational Velocity Calculation</i>	36
CHAPTER 3: RESULTS & DISCUSSION	38
3.1 ANALYSIS OF OUR K-G GIANTS' SPECTRA-DERIVED PROPERTIES	38
3.1.1 <i>Lithium Abundance Evaluation</i>	38
3.1.2 <i>Metallicity Evaluation</i>	38

3.1.3	<i>Rotational Velocity Evaluation</i>	39
3.2	INVESTIGATING CORRELATIONS BETWEEN SPECTRA PROPERTIES AND LITHIUM ABUNDANCE	41
3.2.1	<i>Correlations Between Lithium Abundance and Calculated Stellar Parameters</i>	42
3.2.2	<i>Correlations Between IR Excess and Calculated Stellar Parameters</i>	44
3.4	COMPARISONS TO “ON INFRARED EXCESSES ASSOCIATED WITH LI-RICH K-GIANTS” (REBULL ET AL. 2015).....	45
3.5	CLASSIFYING LITHIUM ENRICHMENT ORIGIN AND PROCESS HYPOTHESES FOR OUR LITHIUM-RICH IR EXCESS K-G GIANTS	46
3.5.1	<i>HB Red Clump Lithium-Enrichment Processes</i>	47
3.5.2	<i>RGB Luminosity Bump Lithium Enrichment Processes</i>	48
3.5.3	<i>AGB Bump Lithium Enrichment</i>	48
CHAPTER 4: CONCLUSION		49
CHAPTER 5: FUTURE WORK & APPLICATIONS		51
BIBLIOGRAPHY		53
APPENDIX A		57
	DOPPLER SHIFT CALCULATION AND GRAPHING PROTOCOL.....	57
APPENDIX B		61
	EVALUATION OF LITHIUM ABUNDANCE VIA FGK LTE GAIA-ESO CURVE OF GROWTH	61
APPENDIX C		63
	PYMOOG METALLICITY EVALUATION USING CHI-SQUARED MINIMIZATION SCHEME	63
APPENDIX D		68
	NEUTRAL IRON LINES’ IDENTIFICATION, FWHM CALCULATION, AND PROJECTED ROTATIONAL VELOCITY SPECUTILS PROTOCOL	68

List of Figures

Figure 1 (A, B): HR Diagrams Depicting Evolutionary Tracks for Stars of Varying Solar Masses..	2
Figure 2 (A, B): HR Plots of Our IR Excess K-G giants.....	19
Figure 3 (A, B): Comparison of Original and Doppler Shifted Spectra for AWI0005zgp.....	24
Figure 4 (A, B): Spectral Fitting Process for AWI0000eg6.....	26
Figure 5: Function Fit of Gaia-ESO FGK Curve of Growth for AWI0000eg6.....	28
Figure 6 (A, B): Input and Output of pyMOOG Automatic A(Li) Function (abfind).....	29
Figure 7: Observed vs. Synthetic Spectrum for AWI0005d61 in the Wavelength Range 6000-6500 Å.....	31
Figure 8: Chi-squared Values vs. Metallicities for AWI0005zgp	34
Figure 9: Determination of Significant Iron Lines for AWI0000qxd Spectra.....	36
Figure 10: Projected Rotational Velocities ($v\sin(i)$) at Each Iron Line for Each Lithium-Rich K-G Giant.....	37
Figure 11 (A, B, C): A(Li) vs. Calculated Stellar Parameters.....	43
Figure 12 (A, B): IR Excess vs. Calculated Stellar Parameters.....	44
Figure 13: Evaluation of A(Li) vs. IR Excess (W1-W4) for Rebull et al. 2015 Objects.....	46

List of Tables

Table 1: K-G Giant Corrected and Uncorrected Mg and (B-R) Values.....	18
Table 2: IR Excess K-G Giant Classifications via HR Diagrams.....	22
Table 3: Evaluation of Mean Doppler Shift for Each Object.....	23
Table 4: Manual vs. Automatic EW and A(Li) Evaluations at 6707.8 Å to Determine Lithium Enrichment in 17 IR Excess K-G Giants.....	30
Table 5: pyMOOG Derived vs. Other Surveys' Photometric [Fe/H] Estimates.....	39
Table 6: Average FWHM and Average vsin(i) Values for Lithium-Rich IR Excess Giants.....	41
Table 7: All Li-Rich IR Excess Giant Identification Parameters.....	47

Chapter 1

Introduction

Stellar evolutionary models predict the behavior of stars throughout their lives and identify expected parameters at various evolutionary phases. Such expected characteristics at specific evolutionary phases include elemental abundances in the stellar atmosphere and nuclear processes fueling the star. Instances of certain stellar anomalies have led astrophysicists to question our developed stellar evolutionary models. One such phenomenon is the presence of lithium enrichment in evolved intermediate-mass giant stars. This investigation will explore the peculiarly high lithium abundances of a set of such evolved giant stars to contribute to the discussion of reevaluating our current models of stellar evolution. Ideally, our results will offer more information into the origin of lithium in these objects and the processes involved in excessive lithium production.

1.1 Evaluating Current Models of Stellar Evolution

Evolution of stars is directly related to the nuclear fusion processes that power them. After nebulae collapse to form protostars, the protostars gradually obtain stable equilibrium and join the main sequence. Main sequence stars generate energy via nuclear fusion of hydrogen atoms in their core. As this fusion begins to form a helium core, main sequence stars like our sun begin to fuse hydrogen in a spherical shell surrounding the core, causing the star to gradually grow and

approach the subgiant phase. As the core exhausts its supply of hydrogen, stars evolve off the main sequence (Laughlin et al. 1997). Eventually, stars reach the red giant phase, and depending on the mass of the star undergo various transitions that will be discussed in the next section. For reference, figure 1 displays the evolutionary tracks of stars of various solar masses on a Hertzsprung-Russell (HR) diagram, with location on the diagram being dependent on a stars' color and luminosity values at evolutionary stages.

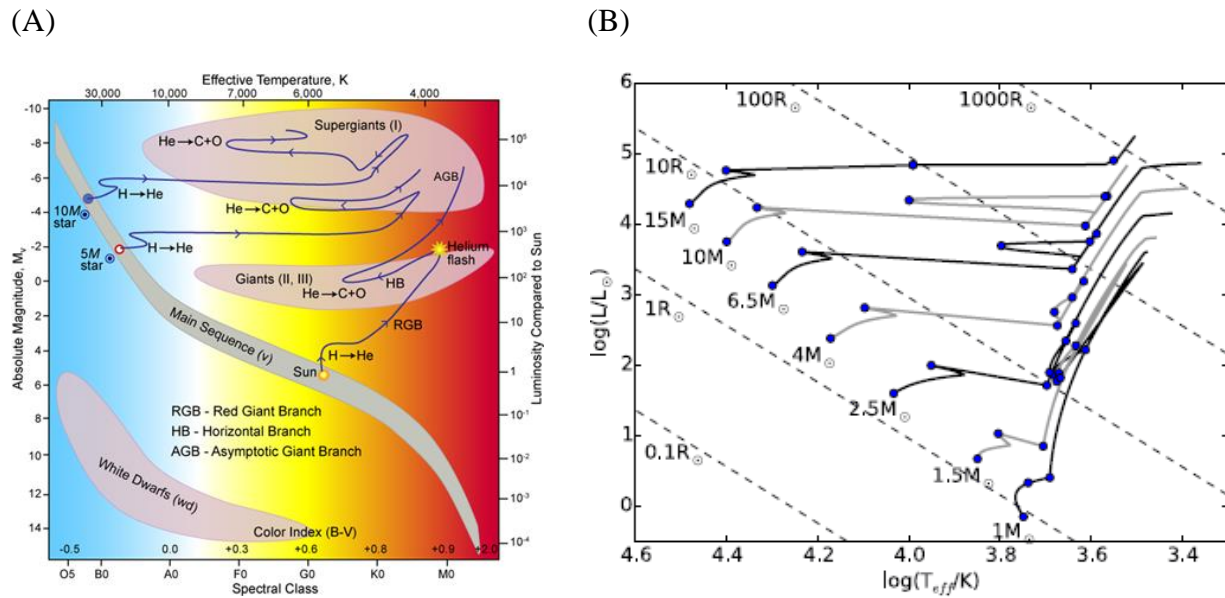


Figure 1: HR Diagram Depicting Evolutionary Tracks for Stars of Varying Solar Masses. Evolutionary tracks of stars of different masses shown in 1A for 10 M_{\odot} , 5 M_{\odot} , and 1 M_{\odot} star and in 1B for 15 M_{\odot} , 10 M_{\odot} , 6.5 M_{\odot} , 4 M_{\odot} , 2.5 M_{\odot} , 1.5 M_{\odot} , and 1 M_{\odot} star. 1A depicts a general Hertzsprung-Russell diagram showing how stars' evolutionary phase is organized via luminosity (absolute magnitude of intrinsic brightness on y-axis) and color (B-V index that determines spectral class and effective surface temperature on x-axis). Diagram via Hollow, Commonwealth Science, and Industrial Research Organization (CSIRO), Australia. 1B depicts an evolutionary track diagram and calculations done by Toonen et al. (2016). Evolutionary tracks plotted using modeled stellar values of $\log(L/L_{\odot})$, or the logarithmic value of luminosity expressed in terms of solar luminosity, and $\log(T_{eff}/K)$, or the logarithmic value of effective surface temperature. Dashed lines represent lines of constant radii derived using Stefan-Boltzmann Law.

1.1.1 General Processes of Red Giant Evolution by Stellar Mass Profile

1.1.1.1 Low-Mass Stars

Low-mass stars are usually identified as being less than 0.5 solar masses (M_{\odot}), or half the mass of our sun, and are characterized as cool, red M-type stars or orange K-type main sequence stars. These stars maintain their location on the main sequence for trillions of years, slowly increasing in temperature and luminosity, yet never undergoing helium fusion due to the small size of their cores. Low-mass stars closer to 0.5 M_{\odot} can evolve into red giants and move from the main sequence to the red giant branch (RGB). However, their expansion is only via hydrogen shell burning around their helium cores, as low-mass star cores are too low in temperature to ignite helium fusion (Hansen et al. 2004). After hydrogen shell burning stops, low-mass stars move off the RGB to become helium white dwarfs.

1.1.1.2 Intermediate-Mass Stars

Intermediate-mass stars, ranging anywhere from about 0.5 to 8 M_{\odot} , are characterized in the range of F, G, and K-type giants. F-type stars are the hottest and yellow in coloration, while K-type stars are the coolest and reddest among intermediate mass stars. Beyond these spectral types, intermediate mass stars are typically red giants in one of two phases of post-main sequence evolution: along the RGB or asymptotic branch (AGB).

Evolved intermediate-mass RGB giants experience gravitational core collapse due to insufficient internal pressure, causing rapid hydrogen fusion around the core and thus a “luminosity bump” or surge in luminosity, as well as expansion of the outer layers of the star. Once the hydrogen around the core fuses to completion, the core’s absorption of the produced helium leads to contraction, ultimately igniting helium fusion. In intermediate-mass giants around 2 M_{\odot} ,

this ignition creates a massive energy release known as the helium flash, causing the star to contract and migrate to the horizontal branch (HB). Many HB giants fall into a region known as the red clump, a stable region of the HR diagram characterized by stars that have finished helium fusion and are undergoing core helium burning (as well as experiencing helium fusion and hydrogen burning in the core-surrounding shell, or intershell).

AGB giants are generally characterized as evolved RGB stars. Having consumed all helium in the core via fusion, AGB giants exhibit hot, inert carbon and oxygen cores with helium fusion and helium burning in the intershell (Hansen et al. 2004). Another shell of hydrogen burning surrounds this shell closer to the stellar surface. Throughout evolution along the AGB, this hydrogen burning shell periodically contributes helium towards the center of the star, generating thermal pulses of energy output from the helium intershell. Thermal pulses are typical of AGB giants between 4 to 7 M_{\odot} . Evolution across the AGB is associated with rapid mass-loss and effective temperature decrease in giants. Eventually, a superwind develops around AGB giants via ejected material from the outer atmosphere, contributing to the most rapid period of mass loss (Quarles 2023). The buildup of circumstellar debris from mass loss leads to intermediate-mass post-AGB stars evolving blueward. As hydrogen and helium burning shells are extinguished, intermediate-mass stars cool to become white dwarf stars, essentially composed of their red giant phases' degenerate carbon and oxygen core.

1.1.1.3 Massive Stars

Massive stars, being anywhere above 8 M_{\odot} , are characterized as O, B, A, and sometimes include early F-type stars. O-type stars are the hottest and brightest stars, known as supergiants, with size and temperature decreasing gradually transitioning to B, A, and early F-type stars. Massive stars contain cores so large that helium ignition does not result in a significant luminosity

increase. Instead, electron degeneracy pressure continues to exceed inward gravitational force, preventing the core from gravitationally collapsing. This leads to heavier and heavier elements fusing, igniting, and forming subsequent shells in the star (Vanbeveren et al. 2009). These objects are not expected to survive evolution to red supergiants and depending on extremity of mass eventually form heavy element white dwarfs or are destroyed via type II supernovae, thus forming a neutron star. For those stars exceeding $20 M_{\odot}$, the sheer amount of mass may result in the star undergoing complete gravitational collapse, forming a black hole.

1.1.2 Lithium Enrichment in Evolved Intermediate-Mass Giants Contradict Current Models of Stellar Evolution

Several phases attributed to intermediate-mass giant evolution contain processes associated with lithium destruction in the star. The transitory helium flash phase of certain intermediate-mass RGB giants is characterized by the outer layers of the stars expanding and cooling, the star's rotation rate slowing, the convection zone deepening, and an initiation of a series of shell-burning and core-burning phases (Rebull et al. 2015). The process of the convection zone deepening brings the material of the stellar surface to the interior through vertical motions, where lithium atoms are brought to deep layers of the star, and they are destroyed via proton capture (Lopez-Valdivia et al. 2018) after exceeding temperatures of $2.5E6$ Kelvin in the stellar interior (Zhang et al. 2020). This process leads to a significant dilution in lithium abundance in these giants. As such, the observance of high amounts of lithium in intermediate-mass RGB and HB giants contradict current models of stellar evolution.

Evolution along the AGB for intermediate-mass giants is associated with thermal pulses, or alternating periods of quiescent hydrogen shell burning and ignition of helium burning in the

helium-rich intershell (Karakas et al. 2014). Periods of helium burning in the intershell during thermal pulses produce short-lived spikes in luminosity, power a convective zone in the intershell, and contribute to “dredge-up” of carbon and helium burning products to the stellar surface as the outer convective envelope moves inwards (Iben 1981). AGB giants above $5 M_{\odot}$ can even experience hot bottom burning, or the development of a deep convective envelope reaching all the way to the top of the hydrogen shell following the formation of a convective zone in the intershell from a thermal pulse. Generally, processes resulting from thermal pulsing are thought to dilute the surface abundance of lithium in AGB giants by not only bringing material from lithium-depleted regions of the stellar interior to the surface via dredge-up but enhancing efficiency of lithium destruction through proton and alpha capture via deep convective mixing. Thus, the observance of high amounts of lithium in intermediate-mass AGB giants also make us question existing models of stellar evolution.

1.2 Identification of Lithium Enriched Disk Detective IR Excess Objects

The Disk Detective citizen project, launched in 2014, was originally designed to find stars with infrared (IR) excess using ALLWISE data from the Wide-Field Infrared Survey Explorer (WISE) mission (Kuchner et al. 2016). IR excess is determined by the difference between W1 and W4 infrared bands from ALLWISE photometric data from the WISE mission. For Disk Detective, IR excess is qualified by the parameter $W1-W4 > 0.25$, however for K5-K9 stars a stricter parameter is imposed of $W1-W4 \gtrsim 0.4$ due to these stellar types having more significant stellar contribution at the WISE wavelengths (Kuchner et al. 2016). The spectral data for these objects was followed up with medium resolution spectral data from the FAST spectrograph on the

Tillinghast 1.5-meter telescope at the Fred Lawrence Whipple Observatory and the REOSC spectrograph at the CASLEO Observatory. The spectra were also combined with distance estimates from the Gaia DR3 release to classify the nature of the Disk Detective objects.

IR excess objects were vetted originally with the goal of identifying young stellar object candidates with debris disks. However, with the incorporation of Gaia's DR3 release distance estimates, the initiative revealed that some of the infrared excess objects were giants, identifying nearly 144 giant star candidates that produced circumstellar material as they evolved off the main sequence (Bans et al. 2024). 21 K-G giants among these IR excess giants showed evidence of lithium line absorption. Generally, 1-2% of all existing K-G giants have been identified as presenting with peculiarly high lithium abundance (Holanda et. al., 2020). Yet out of the 144 infrared excess giants classified through Disk Detective, nearly 15% had the potential to be lithium-enriched (see section 2.3.5), offering the potential for an investigation into origins of lithium enrichment in a highly confident set of IR excess K-G giants with reliable optical spectroscopic data.

The IR excess nature of our set of K-G giants, along with their peculiar lithium enrichment nature, offers an interesting approach and potential for correlations to be found between IR excess and lithium enrichment in the giants. Past research has noted possible links between red giants with overabundant lithium and IR excesses that imply a mechanism of ejection of circumstellar materials and formation of a disk (Rebull et al. 2015). Although lithium enrichment in K-G giants has been investigated along with possible presence of IR excess in those objects, the approach of using highly confident IR excess K-G giants identified through Disk Detective offers a more thorough investigation into this possible correlation.

1.3 Existing Hypotheses for Origins of Lithium Enrichment in Giants

Investigations into this peculiar set of K-G giants aim to uncover potential correlations that may offer evidence in support of the origins of their lithium enrichment. By looking at correlations between quantified lithium abundance and stellar parameters including metallicity and rotational velocity, the origins of the lithium enrichment become clearer. Existing lithium enrichment origin hypotheses for giants include *in situ* enrichment mechanisms and auto-enrichment mechanisms. By analyzing the properties of these identified IR excess K-G giants with lithium abundance, we aim to shed light on various existing theories regarding the causes of lithium enrichment in giant stars.

1.3.1 *In situ* Lithium Enrichment Mechanisms

In situ enrichment mechanisms consider the possibility of an external source of lithium in these enriched giants. Multiple models of external acquisition of lithium have been proposed over the years. These engulfment models invoke some external reservoir of lithium, perhaps from ingestion of a planet, substellar companion, or mass transfer from an AGB companion. As early as 1967, Alexander et al. described favorable circumstances for lithium enrichment via planet engulfment in population II red giants and called for opening the possibilities of origins of lithium enrichment in these giants to go beyond internal nuclear processes and consider external sources (Alexander 1967). Alexander's hypotheses regarding *in situ* lithium enrichment via planetary engulfment could possibly explain presence of lithium enrichment and/or metal-richness in population II red giants, although it is worth noting these metal-poor stars do not typically have many planets.

1.3.1.1 Planet or Dwarf Star Engulfment

Other *in situ* enrichment models that consider external accretion sources like rocky planets include dwarf stars as a potential external source of lithium. One such model describes observational signatures indicative of an accretion process hypothesized to involve planet or brown dwarf star dissipation at the bottom of the convective envelope, in turn accompanied by substantial expansion of the star and bottom burning (Siess et al. 1998). The observational signatures emphasized by Siess to potentially indicate this accretion process include the ejection of a shell and thus a subsequent phase of IR emission, an increase in the lithium surface abundance and stellar metallicity, and spin-up of the star due to deposition of orbital angular momentum (Siess et al. 1998). Some evolutionary models computed in the last few years even suggest the merging of a helium white dwarf star with a red giant branch (RGB) star as the main progenitor of lithium-rich red clump stars (Zhang et al. 2020).

Despite the popularity in external lithium accretion being explained by a giant's engulfment of a lithium rich planet or dwarf star, limitations to this theory have been posed by researchers as well. Certain models elucidate that these external engulfment mechanisms may only explain giants with lithium abundances up to $A(\text{Li}) \approx 2.2$, and giants with higher abundances need alternative explanatory mechanisms (Aguilera-Gomez et al. 2016). Furthermore, planet or dwarf companion ingestion is most likely to occur before the time a star reaches the tip of the RGB, at its maximum radius, making planetary or dwarf star engulfment an unlikely origin hypothesis for lithium-richness in horizontal branch (HB) or AGB giant stars (Kirby et al. 2016).

1.3.1.2 Mass Transfer via Stellar Companion

Beyond the proposed dwarf star or planet engulfment scenarios, another prevailing hypothesis involved lithium-rich material having been accreted from a thermally pulsing asymptotic giant branch (AGB) star companion or ejected nova-explosion material from a novae companion (Jose et al. 1998). Some models postulate the lithium enrichment originating from tidal interactions between binary stars (Siess et al. 1999). Such a close binary system consisting of a white dwarf and a large main-sequence star is defined as a classical nova, involving significant energy release from the main-sequence star to form a circumstellar accretion disk; the abundance levels of intermediate-mass elements in this ejecta, including lithium, were found to be significantly enhanced compared to traditional stellar spectra of main-sequence stars (Jose et al. 1998). Additionally, recent literature proposed that the most likely origin of lithium enrichment in post-RGB stars is from mass transfer with thermally pulsing AGB binary companion (Kirby et al. 2016). Interestingly, this proposal insinuates that lithium-rich post-RGB stars, containing higher surface gravities than HB and AGB stars, acquired mass from the convective envelope of lithium enhanced HB and AGB companion stars, whose own lithium enhancement came from auto-enrichment mechanisms (see section 1.3.2).

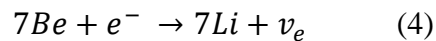
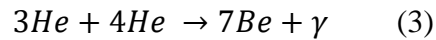
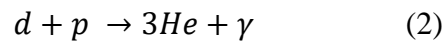
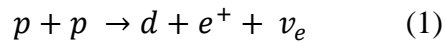
However, these binary system theories are juxtaposed with contradictory findings that binary frequencies among lithium-rich K-giants are found to be normal compared to binary frequencies of typical K-giants (Jorissen et al. 2020), and many observed lithium enriched giants have been observed as isolated field stars, indicating that the formation of lithium enriched giants may not depend on their initial conditions such as involvement in a binary star system (Zhang et al. 2020).

1.3.2 Auto-enrichment Lithium Generating Mechanisms

Auto-enrichment mechanisms are the prevailing theories for origins of lithium enrichment in giants, although the applicability of these mechanisms to all giant stellar objects is widely debated. Auto-enrichment mechanisms imply self-generation of lithium in the star, whether through processes that conserve lithium throughout phases of stellar evolution, produce lithium internally, or via rapid rotation of the star. Existing auto-enrichment mechanisms are generally thought to be short-lived processes correlated to specific stellar evolutionary stage phases.

1.3.2.1 Internal Thermonuclear Production of Lithium

Most prominently accepted is the “Cameron-Fowler conveyor” mechanism, involving an internal thermonuclear production of lithium (Cameron & Fowler 1970). The internal thermonuclear production of lithium considers the 5-step reaction mechanism of the proton-proton-II (pp-II) chain of hydrogen burning in stellar core nuclear reactions:



Most notable are reactions (3) and reaction (4), the fusion of helium-3 and helium-4 nuclei to form beryllium-7, which captures an electron to form lithium-7. Cameron and Fowler proposed that the scarcity of bound K-shell electrons at high temperatures extends the half-life of beryllium-7 from 53 days in terrestrial conditions to 50-100 years, creating a delay that allows for more formation of lithium-7 (Cameron & Fowler 1970). As mentioned in section 1.1.1.2, intermediate-mass giants can exhibit thermal pulses during evolution on the AGB that may lead to mixing of intrastellar

material in the region of pp-II burning (Kirby et al. 2016). Thus, as lithium destruction in reaction (5) is temperature dependent (being more efficient at temperature above $2.5E6$ Kelvin), intrastellar mixing via AGB thermal pulsing could lead to the delivery of freshly synthesized lithium to the surface of the star.

However, as Kirby notes in his 2016 analysis, this conveyor mechanism may not be active in all giant stars; first-ascent RGB stars and less massive AGB stars may have convective envelopes too shallow to activate this conveyor mechanism. Such lithium production and mixing in intermediate-mass stars at the base of the AGB is thought to cease once a strong mean molecular weight gradient has been established between the convective envelope and surrounding nuclear-burning shell, suggesting that such a period of lithium enrichment in stars at this specific evolutionary stage and mass range is short-lived (Charbonnel & Balachandran, 2000).

1.3.2.2 Helium Core Flash

While the Cameron-Fowler conveyor mechanism provides a possible hypothesis for abundant lithium origins in intermediate-mass AGB stars, other proposed auto-enrichment mechanisms suggest correlations between a brief period of lithium enrichment and the helium flash, which typically occurs between the RGB tip and early AGB phases of stellar evolution. Generally, the steps leading up to the helium flash are responsible for the depletion of lithium in a star's evolution (see section 1.1.1.2). However, recent literature suggests the Cameron-Fowler conveyor may operate at the helium core flash in stars around $2 M_{\odot}$, indicating the helium flash could be the explanation for trends of lithium-enriched stars falling in the RGB tip, with the lithium being swiftly destroyed as a clump star evolves to early reaches of the AGB (Kumar et al. 2011). This line of reasoning was supported by Rebull's findings of the RGB tip being the most prominent

region for lithium rich stars, suggesting the lithium enrichment is triggered by the helium flash at the RGB tip (Rebull et al. 2015).

1.3.2.3 RGB Luminosity Bump

Another evolutionary stage attributed to being a potential origin for lithium-enrichment is the luminosity bump of the RGB. One proposed mechanism of lithium production describes intermediate-mass RGB stars as producing lithium during the phase known as the luminosity bump, occurring before the helium flash. The luminosity bump is a phase characterized by the helium core becoming degenerate, causing a temporary halt in core contraction, with the energy generated by helium fusion in the core increasing the luminosity of the star. Theoretically, the luminosity bump involves internal extra-mixing processes, or the first “dredge-up,” to connect helium-3 rich material to the hydrogen-burning shell, enabling lithium production via the Cameron-Fowler conveyor mechanism (Charbonnel & Balachandran, 2000). This model suggests a short-lived period of lithium enrichment as well, predicting that further mixing destroys the freshly synthesized lithium once the carbon isotopic ratio has been lowered.

Interestingly, this first dredge-up of K-giants during the RGB luminosity bump associated with lithium enrichment has also been thought to result in a sudden stellar mass-loss, with the mass-loss proposed to result in the detachment of stellar surface material and the formation of a circumstellar disk (de la Reza et al. 1996). Like that of Charbonnel and Balachandran, de la Reza’s model hypothesizes this lithium enrichment period to be short-lived, spanning 40,000 to 80,000 years, in which the star undergoes changes in its luminosity (i.e. is involved in the luminosity bump RGB phase of stellar evolution).

1.3.2.4 Rapid Rotation

In addition to internal thermonuclear processes, perhaps attributed to specific short-lived periods within phases of stellar evolution, the last prevailing theory of auto-enrichment in lithium enriched giants involves rapid rotation. The correlation between angular momentum and rotational velocity of giants with their lithium abundance has been somewhat explored in past literature. During the early phase of their expansion into giants, smaller stars may transfer angular momentum from their inner regions to their outer surfaces. This process is associated with the movement of intrastellar material, as suggested by Fekel and Balachandran in 1993. In their model, turbulence provided by the transport of angular momentum to the surface provides a mechanism for dredging up freshly synthesized lithium to the surface of the star. This model proposes an alternative method for the movement of newly synthesized lithium, perhaps via Cameron-Fowler conveyor mechanisms, to the surface of stars beyond mixing from thermal pulsing in AGB stars.

A later model proposed a trigger mechanism, facilitated by rapid rotation, for lithium enrichment in RGB tip giants characterized as low-mass stars, post-luminosity bump, that are ascending the RGB (Palacios et al. 2001). The proposed mechanism suggests that beryllium-7 (formed via reaction 3) is diffused into the lower-temperature region between the top of the hydrogen-burning shell and the base of the convective envelope via rapid rotation, allowing beryllium-7 to form lithium-7 via proton capture (see reaction 4). This diffusion and subsequent formation of lithium-7 is thought to result in a significant release of energy in this region as lithium-7 is converted to helium-4 (via reaction 5), triggering a “lithium flash” that turns the region convective, merging with the convective envelope of the star. This mixing process is thought to enrich the outer layers of the star with lithium for a short duration before being destroyed again at the base of the convective envelope. Like Charbonnel and de la Reza’s models, the lithium flash

is thought to lead to an increase in luminosity as well as mass-loss and the subsequent formation of a circumstellar dust shell. Evidently, lithium enrichment being attributed to a short-lived process resulting in mass-loss, formation of a circumstellar shell, and an increase in luminosity is the most popular theory - though a correlation with rapid rotation is up for debate. Theories regarding the origins of the lithium enrichment within the star, though, remain conflicted between *in situ* and auto-generation mechanisms.

1.4 Constructing a Novel Approach to the Lithium Enrichment Discourse

Such previous approaches have prompted this investigation of K-G giants to consider not only IR excess and lithium abundance correlations, but also to construct algorithms to determine stellar metallicity and projected rotational velocity for each object. All these stellar parameters will be compared with spectral type, mass, luminosity, and color values of each star to shed light on the potential origins of the lithium enrichment.

High metallicities correlated to lithium abundance could lend evidence in support of planet or dwarf star engulfment that led to substantial material accretion by the star, particularly for any K-G giants around $2 M_{\odot}$ near the RGB tip. However, low-metallicity values for K-G giants near the RGB tip could insinuate auto-generation Cameron-Fowler conveyor mechanisms as proposed by Kumar et al. 2015. Intermediate-mass K-G giants lying in the luminosity bump could have lithium enrichment attributed to internal mixing associated with evolutionary changes (i.e. helium core becoming degenerate and then igniting, increasing luminosity, and initiating mixing of first dredge-up).

High metallicities correlated to lithium abundance in post-RGB K-G giants could implicate lithium enrichment mechanisms via mass transfer with a companion AGB. Presence of high projected rotational velocities in these objects, with low-metallicities, may lend evidence in support of a lithium flash auto-generation mechanism as proposed by Palacios et al. 2001.

Similarly, high projected rotational velocities correlated to lithium abundance and IR excess could lend evidence in support of the formation of a circumstellar disk around the object because of this external accretion process. Depending on location on HR diagram, low-mass K-G giants in early giant phase (subgiant phase) exhibiting high rotational velocity could provide evidence in support of angular momentum experienced during subgiant phase resulting in lithium enrichment in these stars. This high projected rotational velocity, leading to giants developing more circumstellar material, could explain correlations with high IR excess related to rapid rotation lithium enrichment processes.

By comparing these stellar parameters, this investigation presents a novel approach to not only the origin of lithium enrichment in K-G giants (*in situ* vs. auto-generation), but also the characteristics of the duration and mechanisms of the lithium enrichment process. Indeed, as noted by Drake in 2002 and evident by the existing literature around peculiar lithium enrichment in giants, observational requirement for coupling lithium production to rotation and mass loss has been overlooked or subject to nothing more than speculation up until this point (Drake et al. 2002). In Chapter 2, the methods for undergoing this investigation are discussed.

Chapter 2: Methods

2.1 Constraining Stellar Parameters of Our Set of IR Excess K-G Giants

2.1.1 Obtaining Stellar Effective Temperature via HR Diagram

IR excess K-G giants' spectral types were confidently identified by Bans et al. (2024). Our initial analysis of these 21 IR excess K-G giants involved plotting them on a HR diagram using corrected values of absolute magnitude and color with applied reddening and extinction corrections (see Figure 3). Absolute magnitude (M_g) represents the magnitude of intrinsic brightness, while color was identified by the difference between the magnitudes of the Gaia blue and red bands (B-R). Location on the HR diagram was used to identify differences between giants at different evolutionary states contributing to lithium enrichment and assist in constraining each giants' stellar surface gravity ($\log(g)$). Inherent colors with Gaia extinction corrections were used rather than raw B-R values to get the most accurate HR diagram location for each object. Gaia M_g values, our corrected M_g values, Gaia raw B-R color values, and Gaia inherent B-R color values are displayed in Table 1.

Corrections were applied to M_g using the following relationship between M_g and the interstellar reddening value $E(B-R)$, determined by Wang et al. (2019):

$$M_{g \text{ (corrected)}} = M_g - A_g \quad (6)$$

$$A_g = (1.890 \pm 0.015) * E(B - R) \quad (7)$$

where A_g represents the extinction of Gaia’s G-band. This correction incorporates $E(B-R)$ using Gaia’s B and R bands, where the $E(B-R)$ values were obtained by comparing intrinsic and raw B-R values. The value of 1.89 represents the Gaia band extinction coefficient derived from Gaia’s interstellar averages (Wang et al. 2019).

Zoo ID	M_g	M_g (corrected)	$(B - R)_{\text{raw}}$	$(B - R)_{\text{inherent}}$
AWI0005d61	-0.157	-0.905	1.218	0.823
AWI0000wqx	0.350	-0.231	1.157	0.850
AWI0000qxd	0.385	-0.075	1.193	0.950
AWI000621k	-1.930	-2.766	1.392	0.950
AWI0005yjf	2.578	2.136	1.217	0.983
AWI000004g	0.595	0.226	1.179	0.983
AWI0005dlh	0.580	0.191	1.189	0.983
AWI0000eg6	0.853	0.392	1.227	0.983
AWI00001q1	0.717	0.126	1.296	0.983
AWI00061yb	-3.16	-4.898	1.904	0.983
AWI0000hat	0.805	0.227	1.316	1.010
AWI0005yix	0.905	0.095	1.439	1.010
AWI0000mh2	0.524	0.018	1.367	1.100
AWI0005xy6	-3.149	-4.878	1.898	0.983
AWI0005zgp	1.895	0.747	1.817	1.210
AWI0002b9u	-0.130	-1.904	2.369	1.430
AWI0000t35	-3.871	-4.669	1.852	1.430
AWI0005yly	-3.742	-4.054	0.949	0.784
AWI00059y8	0.555	0.017	1.235	0.950
AWI0005dj7	0.952	0.383	1.284	0.983
AWI0005c3y	0.628	-0.099	1.368	0.983

Table 1: *K-G Giant Corrected and Uncorrected M_g and $(B-R)$ Values.* Stars are identified via Zoo and WISE IDs and referred to by their Zoo IDs throughout this investigation. Reduction in B-R values after applying reddening corrections imply some of our objects are extremely reddened, likely due to circumstellar debris contributing to these objects’ reddening. Additionally, several objects are upwards of thousands of parsecs away, contributing to more reddening and elongation of wavelengths due to significant distance.

Visual analysis of these giants’ stellar spectrum revealed that several contained significant Balmer emission indicated by emission peaks at spectral lines along the hydrogen spectrum associated with transitions between higher energy levels and the second energy level. Balmer emissions are typically associated with young stellar objects in a brief luminous period but could also be a result of circumstellar material that formed around giants following a huge mass loss

(Izotov et al. 2007). Although distance estimates provide significant evidence in favor of these objects being giants, it is worth noting that giants containing Balmer emission are more likely to have been potentially misidentified than giants without Balmer emission (Bans et al. 2024).

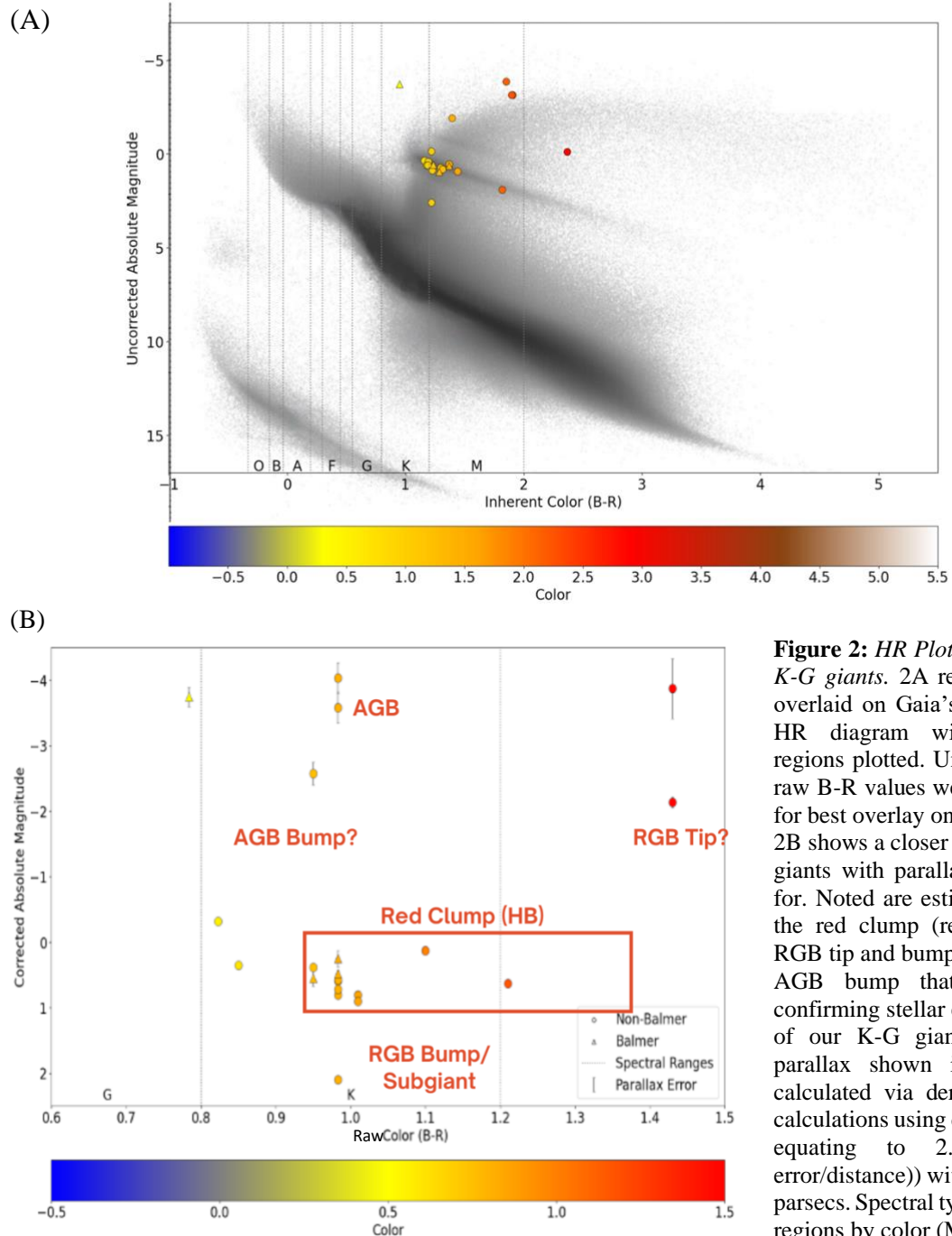


Figure 2: HR Plots of Our IR Excess K-G giants. 2A reveals our HR plot overlaid on Gaia’s uncorrected DR2 HR diagram with spectral type regions plotted. Uncorrected Mg and raw B-R values were used in plot 2A for best overlay on Gaia HR diagram. 2B shows a closer view of our plotted giants with parallax error accounted for. Noted are estimated locations of the red clump (region of HB), the RGB tip and bump, and the AGB and AGB bump that were used for confirming stellar evolutionary tracks of our K-G giants. Error bars of parallax shown in plot 2B were calculated via derivations from M_g calculations using distance (with error equating to $2.17 * (\text{distance error}/\text{distance})$) with distance being in parsecs. Spectral types were plotted as regions by color (Mamajek 2022).

Initial analysis of this set of 21 giants reveals most seem to lie in the red clump within the HB, with two yellow stars left of the red clump possibly also being in this evolutionary stage but appearing bluer due to larger mass values. Beyond this noticeable clump, there appears to be several stars ascending the RGB and AGB branches (ascent being labeled as those branches' "bump"), several stars lying in the AGB, and some approximately near the RGP tip. Evolutionary stage identifications can be seen in Table 2. Notably, one object seems to border-line subgiant phase and RGP bump. The significant reddening of the objects seen in the inherent B-R values versus raw B-R values is further demonstrated by the clear stretch down and to the right of the red clump objects in plot 2A.

Identification of luminosity error as parallax error bars for absolute magnitude values revealed high uncertainty for objects around the AGB region and RGP tip, likely due to these objects' significant distance from us. The observation of some of our objects lying near the RGP tip and most lying in the HB red clump aligns with previous findings that not only found most lithium enriched giants to lie in the red clump, but that hypothesized the lithium enhancement origin of these stars is thus at the RGB tip during helium flash (Deepak & Reddy 2019). Furthermore, the HR plot provides evidence in support of all 21 IR excess objects being giants despite significant Balmer emission, although prompting more investigation into object AWI0005yjf, which appears border-line main sequence.

2.1.2 Estimating Surface Gravity via Absolute Magnitude and Stellar Evolutionary Tracks

Using corrected M_g values, surface gravity ($\log(g)$) values were derived for each K-G giant. Given the relationship between M_g and luminosity (L) with solar brightness ($M_{g\odot}$) and solar luminosity (L_\odot):

$$M_g - M_{g\odot} = -2.5 * \log \left(\frac{L}{L_{\odot}} \right) \quad (8)$$

we can obtain $\frac{L}{L_{\odot}}$. Using the $\frac{L}{L_{\odot}}$ value expressing each objects' luminosity in terms of solar luminosity, we can obtain a radius value in meters for each object using the Stefan-Boltzmann law relating luminosity, radius (R), and temperature (T):

$$L = 4\pi R^2 \sigma T^4 \quad (9)$$

Incorporating our value of $\frac{L}{L_{\odot}}$, T_{eff} for temperature in Kelvin (K), Stefan-Boltzmann constant $\sigma = 5.67\text{E-}8 \frac{W}{m^2 K^4}$, and given that L_{\odot} is approximately 3.8E26 Watts (W), we can thus solve for the radius value in meters (m). Using the equation to calculate surface gravity (g):

$$g = \frac{GM}{R^2} \quad (10)$$

we can input our radius value in centimeters (cm), the gravitational constant $G = 6.67\text{E-}8 \text{ dyne} * \frac{cm^2}{g^2}$ (in CGS units), and solar mass $M_{\odot} = 2\text{E}33$ grams (g) to find the surface gravity of each object.

Using the stellar evolutionary track (Figure 1), upper and lower mass estimates in terms of solar mass were quantified for every object using $\log(T_{\text{eff}})$, a proxy for luminosity identifying placement on the HR diagram. Each mass estimate was used to calculate an upper and lower surface gravity g estimate per object. Finally, taking the $\log(g)$ obtains our upper and lower logarithmic surface gravity values for our giants, which can be seen in Table 2. For later calculations (i.e. involving spectral analysis with input parameters), the average of the upper and lower $\log(g)$ values was used as the determined surface gravity for each object.

Zoo ID	Spectral Type	T_{eff} (K)	Low Est log(g)	High Est log(g)	Class	Location Notes	Est Lum Class	Mass Profile	Low Est Mass (M_{\odot})	High Est Mass (M_{\odot})
AWI0005d6l	G2	6000	2.33	2.55	HB	HB	III	Intermediate	1.5	2.5
AWI0000wqx	G5	5500	2.44	2.67	HB	HB	III	Intermediate	1.5	2.5
AWI0000qxd	G9	5380	2.47	2.69	HB	HB (red clump)	III	Intermediate	1.5	2.5
AWI000621k	G9	5250	1.35	1.57	AGB	AGB bump	I	Intermediate	1.5	2.5
AWI0005yjf	K0	5500	3.39	3.39	RGB	RGB bump/subgiant	IV	Intermediate	1.5	1.5
AWI000004g	K0	5270	2.55	2.77	HB	HB (red clump)	III	Intermediate	1.5	2.5
AWI0005dlh	K0	5270	2.54	2.76	HB	HB (red clump)	III	Intermediate	1.5	2.5
AWI0000eg6	K0	5270	2.62	2.84	HB	HB (red clump)	III	Intermediate	1.5	2.5
AWI00001q1	K0	5270	2.51	2.73	HB	HB (red clump)	III	Intermediate	1.5	2.5
AWI00061yb	K0	5270	0.80	0.93	AGB	AGB/AGB bump	I	Intermediate	3.0	4.0
AWI0000hat	K1	5170	2.52	2.74	HB	HB (red clump)	III	Intermediate	1.5	2.5
AWI0005yix	K1	5170	2.47	2.69	HB	HB (red clump)	III	Intermediate	1.5	2.5
AWI0000mh2	K2	5100	2.41	2.63	HB	HB (red clump)	III	Intermediate	1.5	2.5
AWI0005xy6	K0	5270	0.81	0.94	AGB	AGB/AGB bump	I	Intermediate	3.0	4.0
AWI0005zgp	K3	5000	2.49	2.67	HB	HB (red clump)	III/IV	Low	1.0	1.5
AWI0002b9u	K5	4500	1.43	1.65	RGB	RGB clump	III	Intermediate	1.5	2.5
AWI0000t35	K5	4250	0.74	0.82	RGB/AGB	AGB/RGB tip	I	Intermediate	5.0	6.0
AWI0005yly	G0e	5930	1.35	1.47	AGB	AGB	I	Intermediate	3.0	4.0
AWI00059y8	G9e	5380	2.50	2.73	HB	HB (red clump)	III	Intermediate	1.5	2.5
AWI0005dj7	K0e	5270	2.61	2.84	HB	HB (red clump)	III	Intermediate	1.5	2.5
AWI0005c3y	K0e	5270	2.42	2.64	HB	HB (red clump)	III	Intermediate	1.5	2.5

Table 2: *IR Excess K-G Giant Classifications via HR Diagrams.* Effective surface temperature (T_{eff}) and surface gravity ($\log(g)$) values were constrained given spectral typing via Disk Detective, HR diagram location, and using stellar evolutionary model estimates for mass. Mass profile (low-mass, intermediate-mass, or massive) was documented for each object as well for stellar evolutionary track considerations. Differentiation between AGB and HB or RGB was enhanced by referencing Yerkes spectral classification values (Est Lum Class), I being most luminous and attributed to supergiants (i.e. AGB region stars), II attributed to bright giants, III attributed to normal giants, and IV attributed to subgiants.

2.2 Accounting for Radial Velocity

It is important to account for doppler shift due to radial velocity when evaluating abundance and metallicities using pyMOOG (see section 2.3.2.2 and 2.4.1), as pyMOOG identifies these values using synthetic spectral templates that must be matched with our unshifted spectra. Radial velocity refers to velocity of the object along our line of sight. Negative radial velocity is indicated by blue-shifted wavelengths, meaning the star is moving toward the observer. Positive

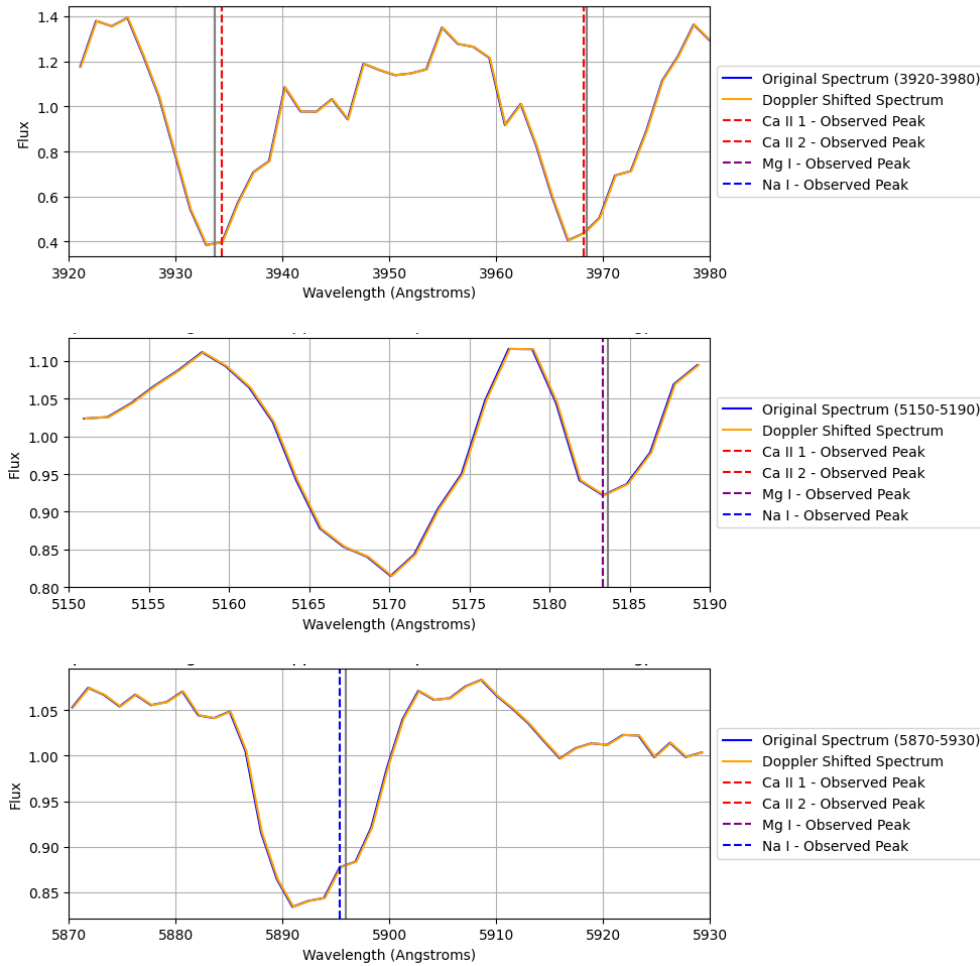
radial velocity is indicated by red-shifted wavelengths, meaning the star is moving away from the observer.

Doppler shifts were evaluated via algorithm constructed using specutils python packages to analyze differences between expected spectral wavelength for notable reference lines versus the observed spectral wavelength the absorbance line occurred at (Specutils Developers 2024). An example spectrum with doppler shift corrections applied is seen in figure 3. Doppler shift and therefore radial velocity were calculated via their relationship with the observed (λ_{obs}) and reference wavelengths (λ), as well as the speed of light c (3E8 km/s) in the following way:

$$\text{Radial Velocity Shift} = \frac{(\lambda_{obs} - \lambda)}{\lambda} * c \quad (11)$$

Average doppler shift across notable reference lines for each object was used to quantify doppler shift due to radial velocity.	Zoo ID	Mean Doppler Shift	Shift Status
Table 3 reveals all our objects' mean doppler shift values and doppler shift status. The full doppler shift protocol can be seen in Appendix A.	AWI0005d6l	-4.77E-5 ± 5.24E-5	Blue-Shifted
	AWI0000wqx	3.16E-5 ± 1.09E-4	Red-Shifted
	AWI0000qxd	-3.50E-5 ± 5.15E-5	Blue-Shifted
	AWI000621k	5.65E-3 ± 6.47E-3	Red-Shifted
	AWI0005yjf	-5.37E-7 ± 5.14E-5	Blue-Shifted
	AWI000004g	1.30E-5 ± 5.58E-5	Red-Shifted
	AWI0005dlh	1.18E-5 ± 1.01E-4	Red-Shifted
	AWI0000eg6	-7.10E-6 ± 1.07E-4	Blue-Shifted
	AWI00001q1	-4.06E-6 ± 1.05E-4	Blue-Shifted
	AWI00061yb	8.62E-3 ± 9.12E-3	Red-Shifted
	AWI0000hat	2.26E-5 ± 5.00E-5	Red-Shifted
	AWI0005yix	-3.81E-5 ± 4.98E-5	Blue-Shifted
	AWI0000mh2	-9.37E-5 ± 7.65E-5	Blue-Shifted
	AWI0005xy6	8.38E-3 ± 9.07E-3	Red-Shifted
	AWI0005zgp	-1.48E-5 ± 1.06E-4	Blue-Shifted
	AWI0002b9u	1.42E-5 ± 5.00E-5	Red-Shifted
	AWI0000t35	-3.81E-5 ± 5.24E-5	Blue-Shifted
	AWI0005yly	6.93E-5 ± 5.00E-5	Red-Shifted
	AWI00059y8	-2.29E-5 ± 1.21E-4	Blue-Shifted
	AWI0005dj7	2.36E-5 ± 8.84E-5	Red-Shifted
	AWI0005c3y	-3.99E-5 ± 9.93E-5	Blue-Shifted

(A)



(B)

Peak Name	Reference Line	Nearest Peak	Doppler Shift
Ca II 1	3933.663	3934.326	0.0001686
Ca II 2	3968.469	3968.162	-7.73e-05
Mg I	5183.604	5183.322	-5.44e-05
Na I	5895.92	5895.353	-9.62e-05
Mean Doppler Shift: -1.4804e-05			
Blue-shifted			

Figure 3: Comparison of Original and Doppler Shifted Spectra for AWI0005zgp. 3A reveals comparisons of original and doppler shifted spectra for this object in three wavelength ranges centered around ionized calcium lines, neutral magnesium line, and neutral sodium line, respectively. The observed peak centers are identified in the legend, and gray vertical lines plotted represent the expected location of the corresponding reference line. 3B exemplifies differences between expected (reference line) and observed (nearest line) wavelengths of notable reference wavelength in stellar spectra of each object. Expected reference wavelengths include those of neutral calcium, neutral magnesium, and neutral sodium with values obtained via the National Institute of Standards and Technology (NIST)'s atomic spectra database (Wright 2002). Hydrogen lines were forgone as reference lines due to some objects having significant Balmer emission.

2.3 Deriving Lithium Abundance

Abundance of elements like lithium in stellar spectra are determined using equivalent widths that measure the strength of the absorption line at the specific wavelength associated with the element. Essentially, the strength of the absorption line depends on the number density of absorbing atoms or ions in the right initial state in the stellar atmosphere and their interaction with photons at specific wavelengths. The lithium abundance determination protocol of this investigation began with different approaches of evaluating the equivalent width of the lithium absorption line to determine robust lithium abundance measurements.

2.3.1 Spectral Line Equivalent Width Evaluation

Equivalent widths (EW) were evaluated through several approaches - via manual calculations with gaussian fits to the line and automatic calculations constructed using python's specutils functionality. Comparisons between manual and automatic calculations provide a check of the viability of automatic spectral analysis features in the specutils package. During this process, spectra were also reviewed for usability. Giants with indistinguishable or highly blended lithium lines were removed from the data set.

2.3.1.1 Manual Equivalent Width Evaluation via Specutils Gaussian Fit

EWs were first evaluated manually at the lithium line at 6707.8 Angstroms (\AA) for each K-G giant. A continuum was fit to the spectra, and then the spectra proceeded to be normalized by dividing over the continuum. A Gaussian fit was applied to the lithium line, which was integrated over to obtain EW. The continuum and Gaussian fit process were completed utilizing spectral fitting tools from the specutils Python package (see Figure 4). Visualization of the lithium absorption line in relation to nearby lines like that of calcium served as a necessary check to

evaluate likelihood of lithium line blending that would leave it unviable for lithium abundance determinations. This usability checks identified AWI00061yb, AWI0005xy6, AWI0005ly and AWI0000mh2 as being unviable for lithium abundance determinations, reducing our giant set to 17 stars.

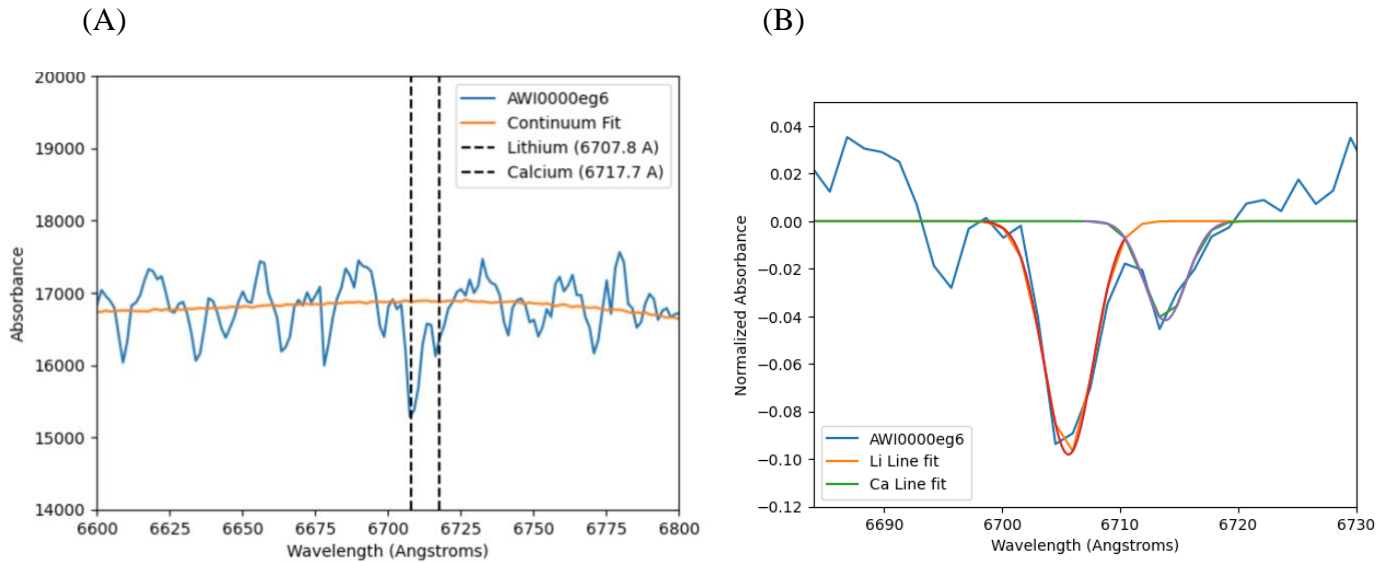


Figure 4: *Spectral Fitting Process for AWI0000eg6.* 4A displays the continuum fit around lithium and calcium absorption lines for this K0 giant, generated by fitting a high order Hermite polynomial to the spectral data points via specutils. 4B displays the continuous Gaussian fits of lithium and calcium absorption lines for the same object. Spectra displayed do not have radial velocity shifts applied.

2.3.1.2 Automatic Equivalent Width Evaluation via Specutils

Following manual calculation and integration of the lines' EWs, the specutils automatic EW function was used. Upon fitting a 200-degree Hermite spline model, the formatted, normalized spectra of each giant was given as an input into the EWauto function, as well as identified left and right wavelength boundaries for the lithium line. These were compared with the manually calculated EWs as a form of verification (see Table 4).

2.3.2 Lithium Abundance Evaluation

These different approaches of evaluating the EWs of the lithium absorption lines of the IR excess K-G giants allowed for the identification of indistinguishable lithium absorption lines, narrowing this set to 17 giants. With this narrowed set, several lithium abundance protocols were explored to quantify each giants' levels of lithium enrichment.

2.3.2.1 Manual Lithium Abundance Evaluation via Gaia-ESO Curve of Growth

Using the lithium equivalent width values and spectral parameters including T_{eff} and $\log(g)$, lithium abundances ($A(\text{Li})$) was first evaluated manually using FGK standard local thermodynamic equilibrium (LTE) curves of growth generated from the Gaia—ESO survey (Gaia Collaboration et al. 2019). LTE models constructed for FGK stars simulate the physical conditions (i.e. T_{eff} , $\log(g)$, etc.) of such stars, generating synthetic spectra for various lithium abundance inputs. By plotting the observed lithium lines' EWs against the physical conditions properties of various synthetic spectra of different $A(\text{Li})$ values, the best lithium abundance value can be generated (see Figure 7). Curve of growth evaluation attached in Appendix B. Although useful, unfortunately this kind of curve of growth method relies on assumptions of LTE and one-dimensional modeling of stellar atmospheres, potentially misrepresenting the complex conditions of real FGK stars, particularly those possibly involved in short-lived lithium enrichment periods. Additionally, this manner of abundance evaluation assumed solar metallicity as a $[\text{Fe}/\text{H}]$ input value for all objects, as this method preceded the creation of a metallicity evaluation algorithm.

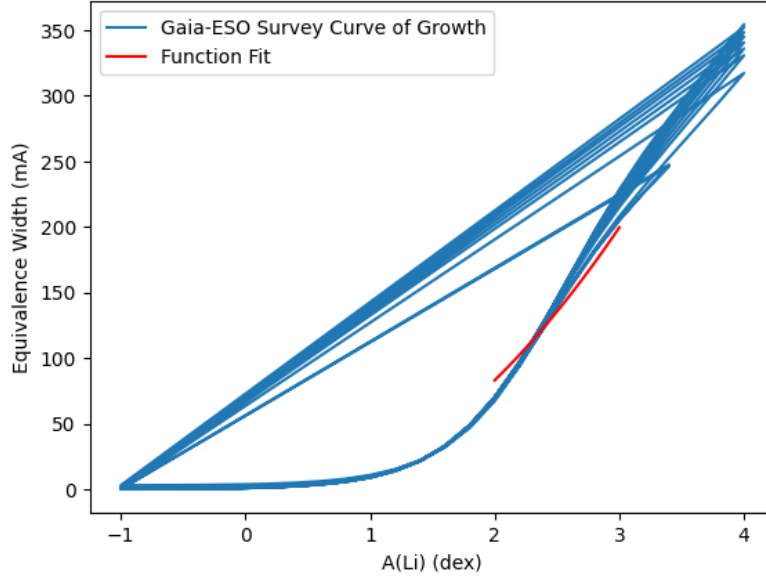


Figure 5: *Function Fit of Gaia-ESO FGK Curve of Growth for AWI0000eg6.* This curve of growth was generated using $\log(g) = 2.5$, $T_{\text{eff}} = 5250$ K, $A(\text{Li})$ measurements attributed to those physical parameters via Gaia-ESO survey calculations, and an input EW of around 520 mÅ. Plotted function fit was applied to derive $A(\text{Li})$ for K-G giants by lithium line EW. $A(\text{Li})$ values are expressed in units of dex, referring to a logarithmic scale that expresses abundances like lithium relative to hydrogen. $\log(\text{EW})$ is assumed to grow with the logarithmic value of the column density, or abundance, of lithium ($\log(A(\text{Li}))$). We assumed this regime when generating a positive correlation quadratic fit when interpolating the curve of growth. This assumption was determined to be less accurate after full metallicity calculations (see section 2.4). Best abundance calculation via curve of growth can be seen in Appendix B.

2.3.2.2 Automatic Lithium Abundance Evaluation via pyMOOG

Spectral synthesis software adapted for python (pyMOOG) was used to construct an automatic lithium abundance generating algorithm. Approaching lithium abundance calculations using pyMOOG offered a novel method of spectral analysis related to K-G giant lithium enrichment, with improved model-fitting and abundance analysis automation, as well as flexibility in customization of these procedures (Jian 2023). pyMOOG's `abfind` function force-fits abundances to EWs, taking specific input parameters and automatically outputting numerous values including abundance in units of dex (see Figure 6). The benefit of using the `abfind` function is that it allows for the $A(\text{Li})$ calculation of multiple wavelengths unlike the manual curve of growth function fits. In this case, beyond the 6707.8 Å line, the 6103.6 Å lithium line was

investigated as well (though significant blending of this line in most of our spectra ruled this lithium line as less reliable). Results of our automatic abundance scheme were compared with manually calculated lithium abundances as a form of verification (see Table 4). The qualifications for whether a star was identified as lithium rich or super lithium rich relied on the abundance value; $A(\text{Li}) > 1.5$ dex was classified as lithium rich, while $A(\text{Li}) > 3.2$ was classified as super lithium rich (Gao et al. 2022).

(A)

```
# Create line list
wavelength_values = [peak_center_1, peak_center_2]
ID_values = [3.0, 3.0]
EP_values = [1.848, 0.0]
log_gf_values = [0.184, 0.167]
C6_values = [0.0, 0.0]
D0_values = [0.0, 0.0]
EW_values = [float(EWauto1.value) * 1000, float(EWauto2.value) * 1000]

table_data = list(zip(wavelength_values, ID_values, EP_values, log_gf_values, C6_values, D0_values, EW_values))

line_list_file = 'line_list.txt'

with open(line_list_file, 'w') as file:
    file.write("lithium line list\n")
    for row in table_data:
        formatted_row = " " + " ".join(f"{item:>5}" for item in row).strip() + "\n"
        file.write(formatted_row)

# Run abfind to calculate lithium abundance for line_list wavelengths
ab = pymoog.abfind.abfind(teff, logg, metallicity, line_list = line_list_file)
ab.prepare_file()
ab.run_moog()

# Read results
with open(ab.rundir_path + 'MOOG.out2', 'r') as file:
    abfind_content = file.readlines()

ab.read_output()

print("\n RESULTS: \n")
print(ab.abfind_res)
```

(B) RESULTS:

{3.0:	wavelength	ID	EP	logGF	EWin	logRWin	abund	delavg
0	6103.6	3.0	1.848	0.184	141.97	-4.633	4.766	0.484
1	6707.8	3.0	0.000	0.167	247.94	-4.432	3.799	-0.484}

Figure 6: *Input and Output of pyMOOG Automatic A(Li) Function (abfind).* 6A denotes the structure of pyMOOG’s abfind function via Jian’s pyMOOG documentation, which requires several input parameters. 5000 is an inputted Teff, 4.0 is inputted log(g), 0.0 is inputted metallicity, and line_list must be an imported file with: unique identifier for spectral line (ID), excitation potential of the lower energy level of the transition associated with the spectral line in units of eV (EP), the log of the oscillator strength (log(gf)), Van der Waals damping (C6), dissociation energy (D0), and equivalent widths obtained from the Gaussian fits in units of mÅ (EW). 6B denotes an example output of abfind for AWI0000hat, which is stored as a dictionary with these outputs: ID, EP, (log(gf)), EW, the log of the residual width of the line (logRWin), abundance in dex (abund), and the average abundance difference (delavg).

Zoo ID	Gaussian Fit EW (mÅ)	Specutils EWauto (mÅ)	Gaia-ESO CoG A(Li) (dex)	pyMOOG abfind A(Li) (dex)
AWI0005d6l	273.843	230.119	2.893	3.812
AWI0000wqx	404.435	361.265	3.797	3.364
AWI0000qxd	265.471	244.146	3.159	3.542
AWI000621k	399.763	384.650	3.623	4.984
AWI0005yjf	84.381	77.526	1.325	1.917
AWI000004g	482.669	454.455	4.052	3.414
AWI0005dlh	488.299	446.545	4.080	4.080
AWI0000eg6	519.426	495.552	4.229	4.492
AWI00001q1	437.164	405.637	3.964	3.799
AWI0000hat	463.437	422.654	3.660	2.946
AWI0005yix	522.958	501.804	3.977	3.952
AWI0005zgp	613.965	559.934	4.126	3.358
AWI0002b9u	406.869	360.576	2.610	1.780
AWI0000t35	723.806	693.645	4.890	3.545
AWI00059y8	713.407	621.428	5.303	4.236
AWI0005dj7	237.072	195.114	2.809	2.452
AWI0005c3y	441.448	391.102	3.847	3.247

Table 4: Manual vs. Automatic EW and A(Li) Evaluations at 6707.8 Å to Determine Lithium Enrichment in 17 IR Excess K-G Giants. Manual EW values were generated via integration over gaussian fit, auto EW values were generated via autoEW specutils functionality, manual A(Li) values were generated via Gaia-ESO LTE curves of growth for FGK stars, and auto A(Li) values were generated via pyMOOG abfind functionality. Li-rich qualifiers are highlighted in yellow while super Li-rich qualifiers are highlighted in orange. Ultimate lithium enrichment qualifications are those determined via pyMOOG indicated in column 5. Auto EW function was entirely unsuccessful for AWI000621 due to weak spectral lines; A(Li) values for this giant used manual EW value only.

2.4 Deriving Metallicity

Metallicities were found by utilizing pyMOOG as well, to generate the best-fit spectral template per spectra. This method of calculating metallicity with pyMOOG, as opposed to photometrically estimated metallicities such as those accessible from Gaia databases, is more reliable for stars with IR excess. Photometric estimates can be affected by many factors relating to IR excess in spectra. Circumstellar material that could be altering observed flux, spectral degeneracy from IR excess K-G giants mimicking spectral features of other stars, and variability in the luminosities of IR excess K-G giants possibly undergoing short-lived luminous, lithium-

producing phases all can contribute to inconsistent photometric estimates. Thus, Gaia photometric estimates' accuracy is doubtful given the IR excess nature of these objects, making spectroscopic analysis techniques via packages like pyMOOG offer a more direct and reliable means of determining metallicity by directly analyzing detailed spectral features.

2.4.1 Generating Synthetic Spectra Using pyMOOG

Synthetic spectra using every available metallicity value in the pyMOOG data banks were generated with the stellar parameters (T_{eff} , $\log(g)$) for each giant (see Figure 7). Notably, the previously calculated doppler shift values for each spectrum were an input parameter for the synthetic spectra for improved accuracy in generation given stellar parameters. By comparing the fit of the synthetic spectra to the observed, the synthetic spectra with the metallicity value most likely correlated with each giant was found using a chi-squared minimization scheme.

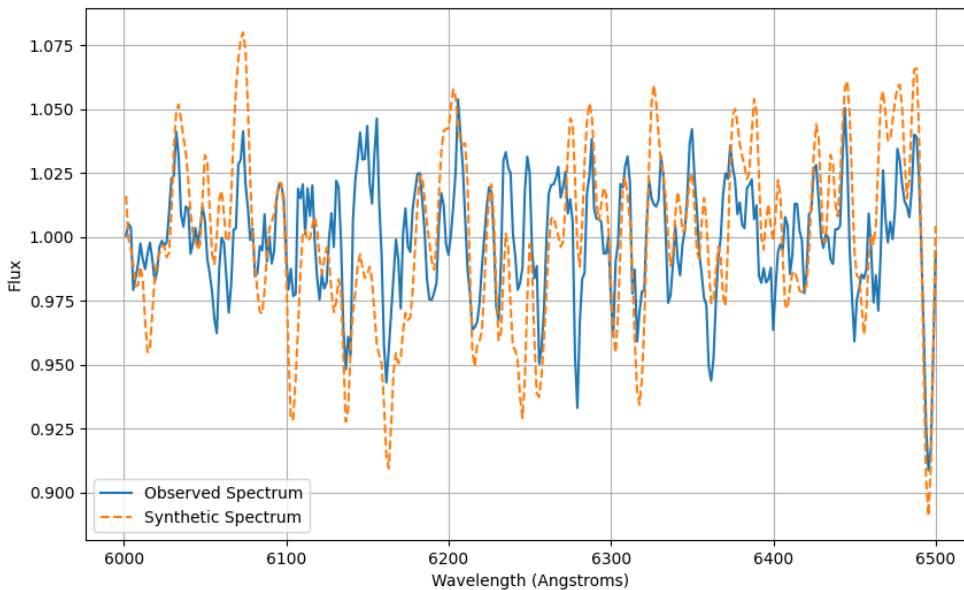


Figure 7: *Observed vs. Synthetic Spectrum for AWI0005d61 in the Wavelength Range 6000-6500 Å.* Synthetic spectra were generated using MARCS model atmosphere data, with input parameters of nearest T_{eff} , nearest $\log(g)$ value, instrumental resolution, and minimum and maximum wavelength. The algorithm then steps through different metallicity values that create the synthetic spectra with the most agreement.

pyMOOG data banks utilize either MARCS (Model Atmospheres in Radiative and Convective Scheme) or Kurucz model atmosphere data to generate synthetic spectra. Experimenting was done between these data values used by pyMOOG to construct the synthetic spectra, given slight differences in the model atmospheres generated by each. MARCS data is computed using a radiative-convective scheme assuming LTE and considering both radiative and convective energy transport in stellar atmospheres. Although this scheme is beneficial in accurately modeling the atmospheric structure and temperature profiles of giants, the computational complexity of the scheme makes it more inefficient. Kurucz, or ATLAS9, models are computed using a one-dimensional plane-parallel approach and assume LTE. Although Kurucz models provide an efficient means of developing a comprehensive grid of synthetic spectra that considers atomic and molecular line profiles of different star types, its one-dimensional approach may not capture the full complexity of convective processes in giant stars. Ultimately, analysis was conducted using MARCS data in anticipation of more accurately generated synthetic spectra to identify optimal metallicities for each star.

2.4.2 Developing the Chi-Squared Minimization Scheme

Although it was the flexible nature of pyMOOG that allowed for the construction of more adept pyMOOG algorithms in this investigation, like automatic A(Li) calculations and generation of synthetic spectra for metallicity evaluation as just described, the adaptability of pyMOOG and limited documentation given its recent construction led to much troubleshooting in evaluating pyMOOG's ability to accurately identify metallicity via the chi-squared minimization scheme. Our scheme found a chi-squared value that showed the goodness of fit between observed and synthetic spectra; our chi-squared values were the normalized different between observed and synthetic spectral template fits (see Appendix C). Due to the variability within each giants' spectra across

the entire range of wavelengths, the chi-minimization scheme was constructed to analyze metallicities across 3 distinct wavelength ranges: 5000-5500 Å, 5500-6000 Å, and 6000-6500 Å (see an example in Figure 8). The wavelength range with the lowest chi-squared value, indicating least discrepancy between observed and synthetic spectra and thus the best fit, was used to identify the truly best metallicity values for each object.

The chosen wavelength ranges purposely exclude significant absorption lines with potential noise that could be affecting the chi-squared evaluation, including telluric lines. Telluric lines are absorption or emission features that arise due to Earth's atmosphere that could contaminate stellar spectra, including an oxygen line at 6850 Å. These ranges also excluded significant features such as the carbon-hydrogen G-band around 4300 Å and titanium-oxide dips around 5000 Å to allow for better analysis of the spectral features of interest (lithium and other metal lines for accurate metallicity evaluation). Unfortunately, MARCS model atmospheres only have surface gravities in increments of 0.5; thus, the metallicity chi-minimization scheme had to find the nearest MARCS surface gravity to the actual calculated surface gravity, although discrepancies are unlikely given surface gravity is likely accurate +/- 0.5.

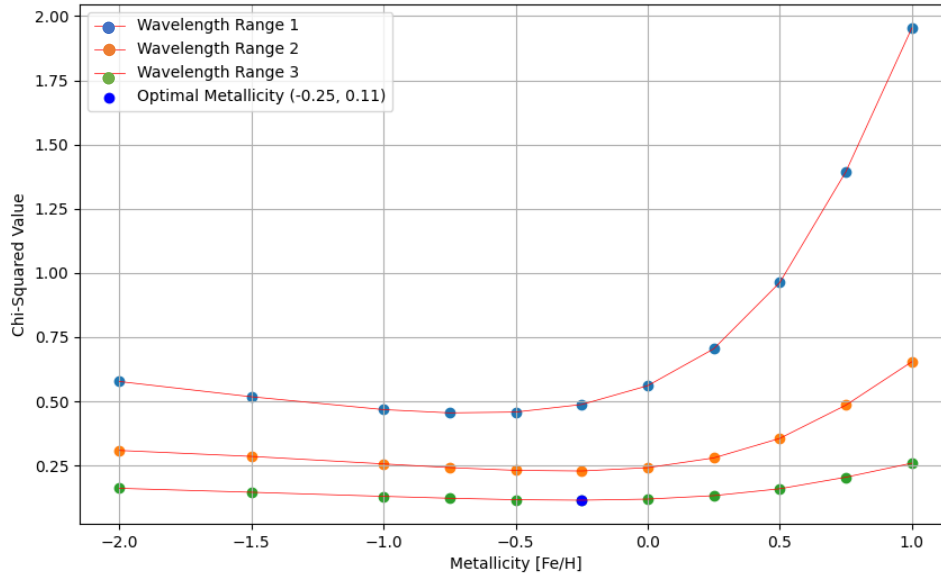


Figure 8: *Chi-squared Values vs. Metallicities for AWI0005zgp.* Chi-squared goodness of fit test, often used in spectral analysis, compares goodness of fit between synthetic and observed spectra. Degrees of freedom are therefore determined via the number of flux values minus 1, as observed and model flux values are compared across the range of wavelengths, with each observed flux value contributing one degree of freedom to the chi-square calculator. As shown above, for object AWI0005zgp, least discrepancy between observed and synthetic flux values was in wavelength range 3 (6000-6500 Å), with the identified best metallicity value in that range being identified as optimal metallicity for this object. Error was found by finding the standard deviation between best metallicities of each wavelength range.

2.5 Deriving Projected Rotational Velocity via Iron Lines’ Full-Width Half Max Values

Projected rotational velocities were investigated for these lithium-rich IR excess giants to evaluate existing hypotheses related to the origin of lithium enrichment in these stars. Project rotational velocities give an idea of whether stars experienced or are experiencing spin-up due to the deposition of angular momentum compared to expected rotational velocities of stars at these evolutionary stages. Generally, younger stars are expected to rotate faster due to angular momentum conservation during the formation process, while older stars may have experienced angular momentum loss through stellar winds or magnetic braking. Thus, projected rotational

velocity values larger than expected could insinuate spin-up due to internal angular momentum redistribution processes or external engulfment.

2.5.1 Determining Significant Iron Lines

A common approach to calculating rotational velocities for objects via spectra is using the full width half maximum (FWHM) values for several iron lines. Iron lines are often well-defined in stellar spectra and indicative of rotational velocity via broadening. Stellar rotation affects iron line width through doppler broadening; as surface material moves toward or away from the observer, shifts in the wavelengths of absorbed iron wavelengths can be quantified via iron lines' FWHM. Thus, FWHM measurements of iron lines provide a robust measure of line broadening contributions via rotational velocity.

Using known neutral and ionized iron lines documented by Holanda et al., our lithium-enriched IR excess K-G giants' spectra were analyzed for substantial iron absorbance. Evaluation of the spectra revealed four prominent iron lines as having significant lines for FWHM calculations: neutral iron (Fe I) at 5916.25 Å, Fe I at 6188.00 Å, Fe I at 6240.65 Å, and Fe I at 6574.23 Å. These prominent absorption lines are exemplified in figure 9.

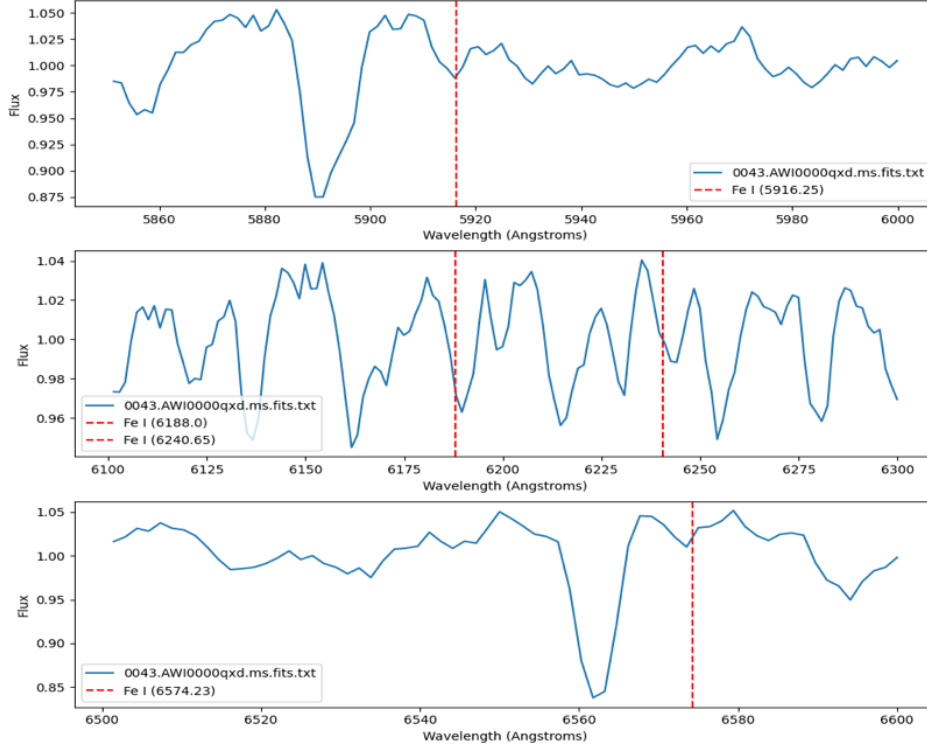


Figure 9: *Determination of Significant Iron Lines for AWI0000qxd Spectra.* Lines appear to be somewhat weak. Differences in FWHM between iron lines are visually apparent based on this plot, emphasizing uncertainty in the average FWHM value derived from iron lines of each spectra.

2.5.2 FWHM and Project Rotational Velocity Calculation

FWHM calculations were done using specutils' FWHM function, after accounting for each spectrum's doppler shift. This function (`specutils.analysis.fwhm`), with given input parameters of spectrum and regions to evaluate, finds the maximum of the spectrum, locates the point closest to half-maximum on either side of the maximum, and measures the distance between (Specutils Developers 2024). These FWHM values are then used to estimate the projected rotational velocity $v \sin(i)$, where v is the rotational velocity, and i represents the inclination angle of the rotating star's axis to the line of sight. This computation is done given the following formula:

$$v \sin(i) = \left(\frac{\sqrt{(FWHM)^2 - (FWHM_{error})^2}}{\lambda_0} \right) * \left(\frac{c}{2} \right) \quad (12)$$

where λ_0 represents the central wavelength of the spectral line, $FWHM_{error}$ represents instrumental broadening, and c is the speed of light. This formula is derived from the relationship between the FWHM of a spectral line and the rotation of the emitting source:

$$FWHM = \left(\frac{2v \sin(i)}{c} \right) * \lambda_0 \quad (13)$$

Projected rotational velocities $v \sin(i)$ must be used as proxies for rotational velocities v because the inclination angle i cannot be directly determined from the spectrum, thus projected rotational velocity values consider potential observational biases and instrumental effects. The calculated projected rotational velocities for each lithium-rich object are visualized in figure 10. The average projected rotational velocity across all iron lines was used as the final determination of projected rotational velocity. Full specutils protocol to evaluate both can be seen in Appendix D.

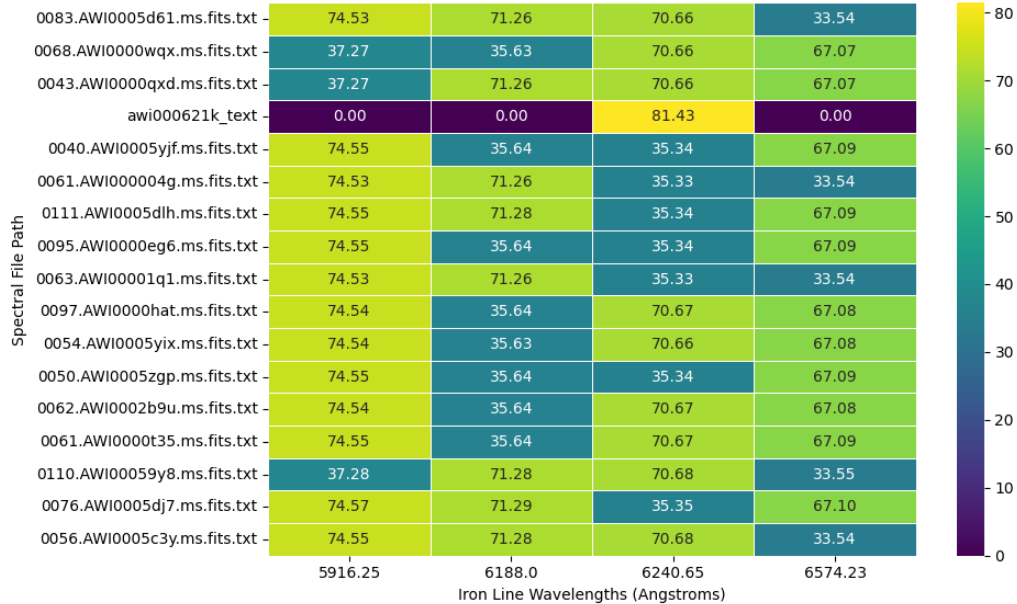


Figure 10: Projected Rotational Velocities ($v \sin(i)$) at Each Iron Line for Each Lithium-Rich K-G Giant. Heatmap plotting feature used to visualize discrepancies and variations in projected rotational velocities across iron lines and spectra. Projected rotational velocities are in units of kilometers per second.

Chapter 3: Results & Discussion

3.1 Analysis of Our K-G Giants' Spectra-Derived Properties

3.1.1 Lithium Abundance Evaluation

As displayed in table 3 following the automatic lithium abundance evaluation via specutils algorithms, 13 of our objects were identified as super lithium-rich and 4 as lithium-rich. These odds significantly contrast existing statistical estimates on prevalence of lithium enrichment in K-G giants. Large survey programs offer statistics emphasizing the rarity of lithium-rich giant occurrence: Gaia-ESO survey predicts around 0.9% of all normal giants will have $A(\text{Li}) > 1.5$ dex (Casey et al. 2016), RAVE survey predicts 0.8% (Ruchti et al. 2011), and SDSS and GALAH predict 0.2-0.3% (Martell & Shetrone 2013). 12% of our IR excess giant candidates were lithium-rich, emphasizing that approaching lithium abundance investigations from an IR excess perspective seems to offer higher likelihood of identifying giants undergoing peculiar, short-lived periods of lithium enrichment related to generating IR excess.

3.1.2 Metallicity Evaluation

The chi-minimization scheme method of calculating metallicity with pyMOOG serves to provide more reliable metallicity values than photometrically estimated metallicities accessible from Gaia databases. To quantify this, the pyMOOG generated metallicities, and associated chi-squared values, were compared to available Gaia metallicity values (see Table 5). Metallicity values are expressed as a logarithmic ratio of iron to hydrogen abundance $[\text{Fe}/\text{H}]$, providing a convenient way to compare the metal content of stars with respect to our sun (solar metallicity = $[\text{Fe}/\text{H}]_{\odot}$). Negative $[\text{Fe}/\text{H}]$ values generally indicate metallicities less than $[\text{Fe}/\text{H}]_{\odot}$, with positive $[\text{Fe}/\text{H}]$ values indicating a metallicity greater than $[\text{Fe}/\text{H}]_{\odot}$. Interestingly, the metallicities derived

via pyMOOG reveal that every lithium-rich object is somewhat metal-poor, displayed by their negative optimal metallicity value. The lack of metal abundance in these stars, unfortunately, dampens the validity of several lithium enrichment process hypotheses thought to be correlated with high metallicity values, such as dwarf star or planetary engulfment.

Zoo ID	pyMOOG [Fe/H]	Gaia [Fe/H]	LAMOST [Fe/H]	APOGEE [Fe/H]	RAVE [Fe/H]
AWI0005d61	-0.25 ± 0.29	-0.20			
AWI0000wqx	-0.75 ± 0.38				
AWI0000qxd	-0.50 ± 0.25				
AWI000621k	-2.00 ± 0.29	0.05			-0.37
AWI0005yjf	-1.00 ± 0.29	-0.15			
AWI000004g	-0.75 ± 0.38			-0.39 ± 0.01	
AWI0005dlh	-0.50 ± 0.25	-0.57			
AWI0000eg6	-0.75 ± 0.43	-0.20	-0.12 ± 0.03	-0.11 ± 0.01	
AWI00001q1	-0.75 ± 0.14				
AWI0000hat	-0.25 ± 0.38				
AWI0005yix	-0.50 ± 0.25		-0.35 ± 0.04		
AWI0005zgp	-0.75 ± 0.38	0.01	-0.05 ± 0.03		
AWI0002b9u	-0.50 ± 0.58	0.27			
AWI0000t35	-2.00 ± 0.00				
AWI00059y8	-0.50 ± 0.29		-0.58 ± 0.02		
AWI0005dj7	-1.50 ± 0.29	-0.17	-0.56 ± 0.05		
AWI0005c3y	-0.75 ± 0.14	-0.54	-0.33 ± 0.07		

Table 5: *pyMOOG Derived vs. Other Surveys' Photometric [Fe/H] Estimates.* Comparisons reveal some agreement, although large discrepancies for certain objects. Notably, objects AWI000621k and AWI0005zgp have the most discrepancy, which may be related to the quality of these objects' spectra; AWI000621k seems to have lower definition, lower resolution spectra and absorption lines compared to the other objects. Gaia photometric metallicity estimates were not available for every object, neither were LAMOST, APOGEE, or RAVE estimates, so comparisons were made when applicable.

3.1.3 Rotational Velocity Evaluation

As mentioned in section 2.5.2, the average projected rotational velocity across all iron lines was used as the final determination of projected rotational velocity. Analysis revealed that FWHM were not very consistent across iron lines, especially for AWI000621k whose peaks seemed

generally smaller than other spectra - possibly attributed to the lower quality of this specific object's CASLEO spectra. Checking specutils automatic determination protocols could assist in narrowing the FWHM values for each iron line; a gaussian fit approach to finding the FWHM value could prove to be more accurate and precise too. The determined average FWHM and projected rotational velocity values can be seen in Table 6. Although the evolution of angular momentum is not entirely known in the astrophysics community, fast rotation is ubiquitous among massive stars, with projected rotational velocity thought to increase for intermediate mass to massive stars as they evolve (Sun et al. 2021). Yet the projected rotational velocities associated with our set of K-G giants would classify them all as rapid rotators, defined by researchers Medeiros & Mayor as stars with $v \sin(i) > 8$ km/s (Medeiros et al. 1999). With this guideline, our objects are very rapidly rotating, exceeding previous literatures' fraction of rapidly rotating intermediate-mass field giant stars in a sample of field giant stars; 1.3% of Medeiros & Mayor's evolved red giant sample exhibited rapid rotation, while less than 0.4% of Sun et al.'s red giant population qualifying as rapidly rotating.

Evidently, this statistical comparison is incredibly biased given Medeiros worked with a population of 432 giants while Sun et al. worked with a population of almost 40,000. However, the likelihood of identifying a group of around 20 K-G giants, all displaying significant IR excess and falling in a similar region of the HR diagram stellar evolutionary track, as also exhibiting rapid rotation raises the question on if our approach to the lithium enrichment dilemma by first evaluating IR excess giants allowed for better understanding of processes involved in lithium enrichment. It is impossible to make definitive conclusions about the rapid rotation associated with these objects without higher resolution spectra.

Zoo ID	Avg FWHM (\AA)	Avg $v\sin(i)$ (km/s)
AWI0005d61	3.309 ± 0.123	79.263 ± 0.543
AWI0000wqx	3.677 ± 0.235	89.106 ± 0.654
AWI0000qxd	3.309 ± 0.346	80.198 ± 0.765
AWI000621k	0.848 ± 0.457	20.358 ± 0.877
AWI0005yjf	3.678 ± 0.568	88.638 ± 0.988
AWI000004g	3.677 ± 0.679	88.096 ± 1.099
AWI0005dlh	3.310 ± 0.789	79.735 ± 1.210
AWI0000eg6	3.678 ± 0.890	88.637 ± 1.321
AWI00001q1	3.677 ± 0.901	88.100 ± 1.432
AWI0000hat	3.678 ± 0.912	88.634 ± 1.543
AWI0005yix	3.677 ± 0.923	88.626 ± 1.654
AWI0005zgp	3.678 ± 0.935	88.637 ± 1.765
AWI0002b9u	3.678 ± 0.946	88.635 ± 1.877
AWI0000t35	3.678 ± 0.957	89.121 ± 1.988
AWI00059y8	3.678 ± 0.968	88.607 ± 2.000
AWI0005dj7	3.311 ± 0.000	79.751 ± 0.000
AWI0005c3y	3.310 ± 0.000	79.284 ± 0.000

Table 6: Average FWHM and Average $v\sin(i)$ Values for Lithium-Rich IR Excess Giants. Standard deviations represent deviations of FWHM and $v\sin(i)$ values between selected iron lines that visually appeared to have rather large discrepancies.

3.2 Investigating Correlations Between Spectra Properties and Lithium Abundance

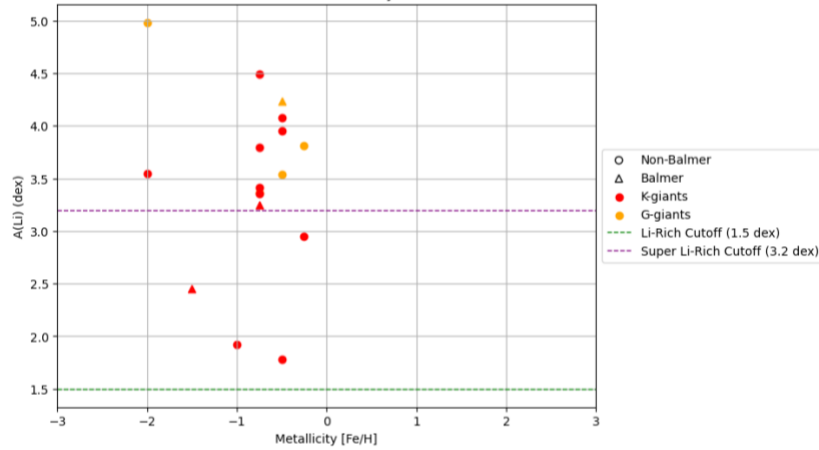
To assess correlations between various spectra properties, empirical associations between properties were visually analyzed via plots. Correlations were investigated between lithium abundance and metallicity, projected rotational velocity, or IR excess (see Figure 11), as well as between IR excess and metallicity or projected rotational velocity (see Figure 12). These objects have all been quantified as having IR excess via difference in W1-W4 bands and lithium-rich or super lithium-rich via $A(\text{Li})$ value (see Table 7). Already, this correlation is unique, as IR excesses are rare in the general K-giant population, as are lithium abundances, suggesting the two parameters are related (Kumar et al. 2015).

3.2.1 Correlations Between Lithium Abundance and Calculated Stellar Parameters

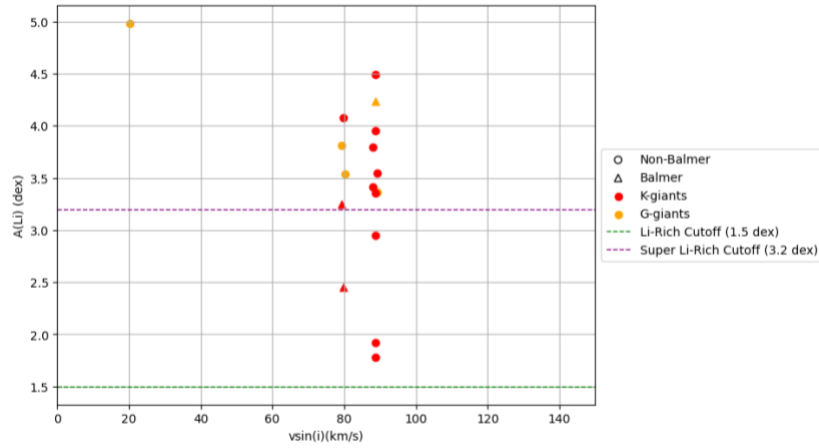
Empirical correlations were explored between $A(\text{Li})$ and calculated stellar parameters metallicity, projected rotational velocity, and IR excess (figure 11). The plots reveal interesting trends; plot 11A and 11B suggest that this set of K-G giants, although displaying varying levels of lithium-richness, tend to have metallicities and projected rotational velocities in the same range of values. This alludes to similar qualities regarding these objects' locations on the stellar evolutionary track, and that these giants may have been observed during similar short-lived processes associated with excessive lithium production/retained lithium abundance at the surface of the star. Relationships between stellar parameters and evolutionary track location is explored further using object identifications, seen in table 6, in section 3.2.3.

The most notable correlation of the plots in figure 11 would have to be $A(\text{Li})$ compared to IR excess. Like conclusions drawn by Rebull et al., plot 11C insinuates that if a giant has large IR excess, it probably has a large lithium abundance as well, but having significant lithium abundance does not necessarily mean the object will have large IR excess (Rebull et al. 2015). However, more so than Rebull's plots, there does seem to be a positive correlation between $A(\text{Li})$ and IR excess, even if it is not incredibly strong. Within our set, the relationship between $A(\text{Li})$ and IR excess suggests the largest lithium abundances are associated with the largest IR excesses. This alludes to a relationship between the processes involved in lithium enrichment also contributing to the IR excess in these stars.

(A)



(B)



(C)

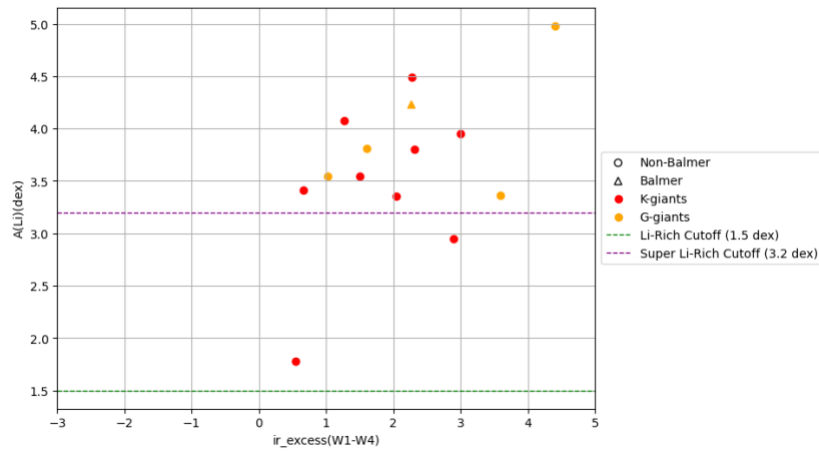


Figure 11: $A(Li)$ vs. Calculated Stellar Parameters. Plot 11A shows $A(Li)$ compared to $[Fe/H]$ values, 11B shows $A(Li)$ compared to $v\sin(i)$ values, and 11C shows $A(Li)$ compared to IR excess values. Spectral type is indicated by plot point color, Balmer emission status remains identified by point type, and the cutoffs for Li-rich and super-Li rich were included as horizontal dotted lines labeled in the legend.

3.2.2 Correlations Between IR Excess and Calculated Stellar Parameters

Empirical correlations were explored between IR excess and calculated stellar parameters of metallicity and projected rotational velocity (figure 12). The plots reveal little correlation, unfortunately. Plot 12A and 12B suggest that this set of K-G giants, although displaying varying levels of infrared excess (and all qualifying as infrared excess), tend to have metallicities and projected rotational velocities in the same range of values. Like the previously explored correlations with lithium abundance, this narrow range of metallicities and projected rotational velocity values allude to similar qualities regarding these objects' locations on the stellar evolutionary track. It is worth noting there seems to be a minute negative correlation between IR excess, with giants' exhibiting lower metallicity values seeming to have the highest IR excess.

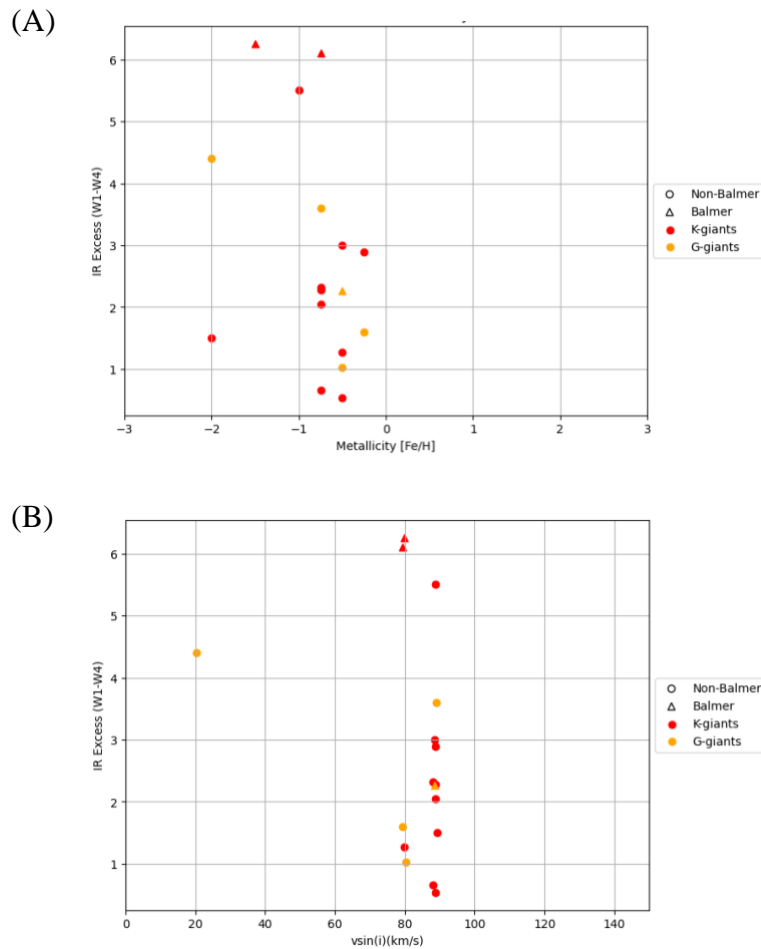


Figure 12: *IR Excess vs. Calculated Stellar Parameters.* 12A shows IR excess, represented by W1-W4, compared to [Fe/H] values, and plot 12B shows IR excess compared to vsin(i) values.

3.4 Comparisons to “On Infrared Excesses Associated with Li-Rich K-Giants” (Rebull et al. 2015)

Structures of plots and investigated correlations were inspired by Rebull et al.’s own 2015 evaluations of correlations alluding to potential origins of Li-enrichment in red giants. However, given GAIA distance parameters that were released following Rebull’s publication, her red giant sample was reevaluated to remove unreliable giants. Using this new, confident giant set, reevaluation of Rebull’s IR excess and $A(\text{Li})$ correlations were reconstructed using the approach of this investigation - identifying IR excess objects and investigating how lithium abundance may be correlated. Figure 13 reveals our reconstruction of Rebull’s $A(\text{Li})$ and IR excess correlation plot, and documented stellar parameters for Rebull’s IR excess, lithium-rich objects are noted in table 6.

Interestingly, all the non-IR excess Rebull objects seem to be clustered in the same region. Although there are a notably fewer points objects after reclassifying giants using distance parameters, Rebull’s set still offers the alluded correlation she originally proposed: if a star has large IR excess, it probably has a large $A(\text{Li})$, but large $A(\text{Li})$ is not explicitly indicative of large IR excess. These relationships made us curious into how $A(\text{Li})$ and metallicity are correlated for her objects, a comparison she did not make in her publication. Interestingly, Rebull’s IR excess lithium-rich objects have an average metallicity value of $[\text{Fe}/\text{H}] = -0.185$, a trend of IR excess lithium abundant giants seeming to be metal-poor as was found in our set of K-G giants. Compared to Rebull’s set of objects, the fact that Disk Detective offers a large supply of highly confident IR excess objects, and the giants among them have a large portion of Li-rich objects, lends support to the likelihood of IR excess giants being lithium enriched

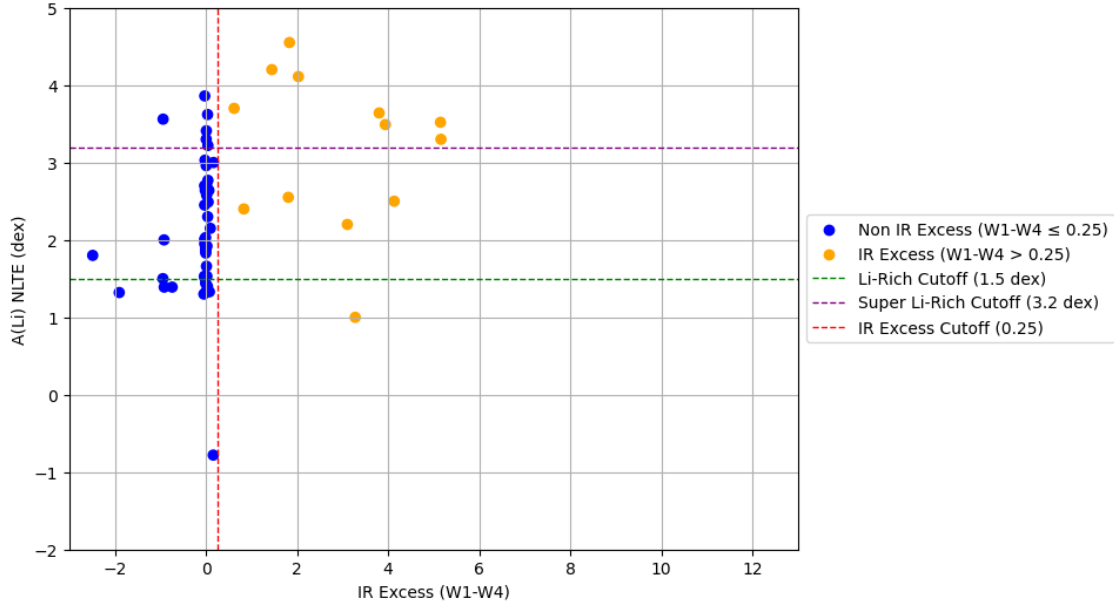


Figure 13: Evaluation of $A(\text{Li})$ vs. IR Excess (W1-W4) for Rebull et al. 2015 Objects. The plot represents all identified giant objects for Rebull, IR and non-IR excess objects, to elucidate a relationship between presence of IR excess and lithium abundance.

3.5 Classifying Lithium Enrichment Origin and Process Hypotheses for Our Lithium-Rich IR Excess K-G Giants

Based on analysis of stellar evolutionary track and calculated stellar parameters, the following are our speculative identification of the origins of lithium enrichment and lithium production processes for our K-G giants following analysis.

Zoo ID	T_{eff} (K)	Avg $\log(g)$	Spectral Type	A(Li)	[Fe/H]	$v \sin(i)$	Avg Est Mass (M_{\odot})	Class	Location Notes
AWI0005d61	6000	2.44	G2	3.812	-0.25	79.263	2.0	HB	HB
AWI0000wqx	5500	2.55	G5	3.364	-0.75	89.106	2.0	HB	HB
AWI0000qxd	5380	2.58	G9	3.542	-0.50	80.198	2.0	HB	HB (red clump)
AWI000621k	5250	1.46	G9	4.984	-2.00	20.358	2.0	AGB	AGB/RGB luminosity bump
AWI0005yjf	5500	3.39	K0	1.917	-1.00	88.638	1.5	RGB	RGB-ascent/subgiant
AWI000004g	5270	2.66	K0	3.414	-0.75	88.096	2.0	HB	HB (red clump)
AWI0005dlh	5270	2.65	K0	4.080	-0.50	79.735	2.0	HB	HB (red clump)
AWI0000eg6	5270	2.73	K0	4.492	-0.75	88.637	2.0	HB	HB (red clump)
AWI00001q1	5270	2.62	K0	3.799	-0.75	88.100	2.0	HB	HB (red clump)
AWI0000hat	5170	0.87	K1	2.946	-0.25	88.634	3.5	AGB	AGB/RGB luminosity bump
AWI0005yix	5170	2.63	K1	3.952	-0.50	88.626	2.0	HB	HB (red clump)
AWI0005zgp	5000	2.58	K3	3.358	-0.75	88.637	2.0	HB	HB (red clump)
AWI0002b9u	4500	2.52	K5	1.780	-0.50	88.635	2.0	HB	HB (red clump)
AWI0000t35	4250	0.87	K5	3.545	-2.00	89.121	3.5	AGB	AGB/RGB luminosity bump
AWI00059y8	5380	2.58	G9	4.236	-0.50	88.607	1.3	HB	HB (red clump)
AWI0005dj7	5270	1.54	K0	2.452	-1.50	79.751	2.0	RGB	RGB clump
AWI0005c3y	5270	0.78	K0	3.247	-0.75	79.284	5.5	AGB/RGB B	AGB/RGB luminosity bump

Table 7: All Li-Rich IR Excess Giant Identification Parameters. Information includes Zoo ID, effective surface temperature, average surface gravity, spectral type, lithium abundance, metallicity, projected rotational velocity, average estimated mass in units of solar masses, HR diagram classification, and notes on evolutionary stage.

3.5.1 HB Red Clump Lithium-Enrichment Processes

- Objects: AWI0005d61, AWI0000wqx, AWI0000qxd, AWI000004g, AWI0005dlh, AWI0000eg6, AWI00001q1, AWI0005yix, AWI0005zgp, AWI0002b9u, AWI00059y8

These stars are all located in the HB or red clump region of the HB, have large surface gravities in the range of 2-3, and have masses ranging from 1.5 to 2.5 M_{\odot} . At this stellar evolutionary stage, these giants have evolved off the main sequence and begun core helium burning, which can lead to internal mixing that may be involved in bringing fresh lithium to the stellar surface, enriching the observed abundance of lithium in these stars.

3.5.2 RGB Luminosity Bump Lithium Enrichment Processes

- Objects: AWI000621k, AWI0005yjf, AWI0006dj7.

These giants lie along the RGB luminosity bump, or ascent of the RGB. A large surface gravity ranges from 1.5 to 4 and mass range from 1.5 to 3 M_{\odot} allude to these intermediate mass objects evolving onto the RGB. This evolutionary stage is associated with convective mixing, particularly during the first dredge-up associated with the luminosity bump. As the convective envelope deepens, this may bring processed material containing lithium to the surface, thus enriching the surface lithium abundance.

3.5.3 AGB Bump Lithium Enrichment

- Object: AWI0000hat, AWI0000t35, AWI0005c3y.

Positioned near the AGB ascent region of the HR diagram, somewhat above the RGP tip region, these objects having a large mass range from 3.5 to 5 M_{\odot} yet a low surface gravity range of around 0.5 to 1 suggests evolution onto the AGB, or the AGB ascent/bump location. During AGB ascent evolution, the second dredge up is likely responsible for generating convective mixing that brings fresh lithium to these objects' stellar surfaces, resulting in significant lithium enrichment.

Chapter 4: Conclusion

Based on high-resolution optical spectra obtained from the FAST spectrograph, we conducted a thorough analysis of lithium abundances in K-G type giant stars, which defy conventional models of stellar evolution by exhibiting large lithium enrichments during their giant phase. Utilizing equivalent widths of the lithium absorption line at 6707.8 Angstroms, we derived lithium abundances and compared them with infrared excess objects. Our investigation focused on stars identified as HB or red clump giants, RGB luminosity bump candidates, subgiants, and stars nearing the RGB tip.

Analyzing potential processes related to the origin of lithium enrichment in these giants required considering specific stellar evolutionary phases attributed to stars of certain masses. For stars in the HB or red clump phase, characterized by masses ranging from 1.5 to 2.5 M_{\odot} , the process of core helium burning likely induces internal mixing, potentially bringing fresh lithium to the stellar surface and enriching observed lithium abundances. Similarly, stars positioned near the RGB luminosity bump, with masses ranging from 1.5 to 4 M_{\odot} , likely experience convective mixing during the first dredge-up associated with the luminosity bump, contributing to lithium enrichment. Objects appearing to ascend the AGB had location confirmed by low surface gravity values and large mass values associated with extreme expansion of the star during this evolutionary phase, before mass loss along the AGB. AGB ascent objects likely have lithium enrichment due to the second dredge up process generating more internal convective mixing.

Our analysis not only quantifies peculiar lithium abundances and infrared excess but also examines stellar spectral lines to derive metallicities and rotational velocities. By comparing our findings with existing literature on lithium-enriched K-G giants, we aimed to uncover potential correlations between additional stellar properties and lithium enrichment origins, and our findings

are supported by existing hypotheses – primarily auto-generation mechanisms association with transitional phases during giant evolution.

Our results contribute to discussions considering reevaluating traditional models of stellar evolution. Further investigations incorporating more observational constraints and robust procedures for gathering stellar parameter information will enhance our understanding of these intriguing phenomena.

Chapter 5: Future Work & Applications

Expanding exploration with PyMOOG by continuum normalizing synthetic spectra and utilizing Kurucz models to refine our understanding of stellar atmospheres and evolutionary processes could provide more robust measurements, especially for metallicities. By leveraging PyMOOG's capabilities, we can delve deeper into the intricacies of stellar spectra, enhancing our ability to extract valuable insights from observed data. Using pyMOOG to investigate other parameters like diffusive mixing coefficients related to processes such as thermohaline mixing could reveal more about the intricate interplay between internal mixing mechanisms and lithium enrichment at the stellar surface.

Further comparative analyses between our identified objects and typical K-G giants in surveys like the Disk Detective Survey hold immense potential for elucidating commonalities and discrepancies in their properties. By leveraging large datasets and advanced data analysis techniques, we can uncover patterns that shed light on the origins and evolution of lithium enrichment in these stars. Continuing the approach of finding established IR excess objects and then looking for associated lithium abundance in other surveys and published sets of spectra could provide further useful insight into correlations between parameters like lithium abundance, IR excess, and metallicity.

Investigating the metallicity of our sample sparks intriguing questions about their formation and evolutionary history. The observation of metal-poor giants prompts speculation about their potential classification as Population II red giants, opening doors to exploring unique stellar populations and their contributions to galactic dynamics and chemical evolution. Furthermore, exploring the link between lithium enrichment in K-G giants and the broader primordial lithium puzzle offers a fascinating avenue for future research. By probing the

mechanisms behind lithium production and destruction in evolving giants, we can contribute valuable insights to one of the fundamental puzzles in astrophysics, shedding light on the early universe's chemical evolution.

Bibliography

1. Alexander, J. B. et al. A Possible Source of Lithium in the Atmospheres of Some Red Giants. *The Observatory* 1967, 87, 238–240.
2. Aguilera-Gómez, C. et al. ON LITHIUM-RICH RED GIANTS. I. ENGULFMENT OF SUBSTELLAR COMPANIONS. *ApJ* 2016, 829 (2), 127. <https://doi.org/10.3847/0004-637X/829/2/127>.
3. Bans, A., et. al. Optical Spectroscopy of 520 Infrared Excess Stars From the Disk Detective Citizen Science Project (2024). *American Astronomical Society*.
4. Cameron, A. G. W. et al. Lithium and the S-PROCESS in Red-Giant Stars. *The Astrophysical Journal* 1971, 164, 111. <https://doi.org/10.1086/150821>.
5. Charbonnel, C. et al. The Nature of the Lithium Rich Giants. Mixing Episodes on the RGB and Early-AGB. 2000. <https://doi.org/10.48550/ARXIV.ASTRO-PH/0005280>.
6. De La Reza, R.; Drake, N. A.; Da Silva, L. Lithium Enrichment–Mass-Loss Connection in K Giant Stars. *The Astrophysical Journal* **1996**, 456 (2). <https://doi.org/10.1086/309874>.
7. Deal, M.; Martins, C. J. A. P. Primordial Nucleosynthesis with Varying Fundamental Constants: Solutions to the Lithium Problem and the Deuterium Discrepancy. *A&A* **2021**, 653, A48. <https://doi.org/10.1051/0004-6361/202140725>.
8. Deepak; Reddy, B. E. Study of Lithium Rich Giants with the GALAH Spectroscopic Survey. *Monthly Notices of the Royal Astronomical Society* **2019**. <https://doi.org/10.1093/mnras/stz128>.
9. Drake, N. A. et al. Rapidly Rotating Lithium-Rich K Giants: The New Case of the Giant PDS 365. *The Astronomical Journal* 2002, 123 (5), 2703–2714. <https://doi.org/10.1086/339968>.
10. Fekel, F. C. et al. Lithium and Rapid Rotation in Chromospherically Active Single Giants. *ApJ* 1993, 403, 708. <https://doi.org/10.1086/172242>.
11. Gagov, S. Reactions of the Arterial Blood Pressure in Changed Haemodynamic Conditions and under the Effect of Bilateral Carotid Occlusion. *Acta Physiol Pharmacol Bulg* 1975, 3–4, 13–21.

12. Gaia Collaboration; et al. *Gaia* Data Release 2: Variable Stars in the Colour-Absolute Magnitude Diagram. *A&A* **2019**, 623, A110. <https://doi.org/10.1051/0004-6361/201833304>.
13. Gao, J.; Zhu, C.; Yu, J.; Liu, H.; Lu, X.; Shi, J.; Lü, G. Li-Rich and Super Li-Rich Giants Produced by Element Diffusion. **2022**. <https://doi.org/10.48550/ARXIV.2210.13152>.
14. Holanda, N. et al. TYC 8327-1678-1: A New Super Lithium-Rich K Giant. *Monthly Notices of the Royal Astronomical Society* 2020, 498 (1), 77–83. <https://doi.org/10.1093/mnras/staa2271>.
15. Iben, I. et al. On the Interior Properties of Red Giants. In *Physical Processes in Red Giants*; Iben, I., Renzini, A., Eds.; Astrophysics and Space Science Library; Springer Netherlands: Dordrecht, 1981; Vol. 88, pp 3–24. https://doi.org/10.1007/978-94-009-8492-9_1.
16. Izotov, Y. I.; Thuan, T. X.; Guseva, N. G. Broad-Line Emission in Low-Metallicity Blue Compact Dwarf Galaxies: Evidence for Stellar Wind, Supernova, and Possible AGN Activity. *ApJ* **2007**, 671 (2), 1297–1320. <https://doi.org/10.1086/522923>.
17. Jorissen, A. et al. Li-Rich K Giants, Dust Excess, and Binarity. *A&A* 2020, 639, A7. <https://doi.org/10.1051/0004-6361/202037585>.
18. José, J. et al. Nucleosynthesis in Classical Novae: CO versus ONe White Dwarfs. *ApJ* 1998, 494 (2), 680–690. <https://doi.org/10.1086/305244>.
19. Karakas, A. I. et al. The Dawes Review 2: Nucleosynthesis and Stellar Yields of Low and Intermediate-Mass Single Stars. *Publ. Astron. Soc. Aust.* 2014, 31, e030. <https://doi.org/10.1017/pasa.2014.21>.
20. Kirby, E. N. et al. LITHIUM-RICH GIANTS IN GLOBULAR CLUSTERS*. *ApJ* 2016, 819 (2), 135. <https://doi.org/10.3847/0004-637X/819/2/135>.
21. Kuchner, M. J.; Silverberg, S. M.; Bans, A. S.; Bhattacharjee, S.; Kenyon, S. J.; Debes, J. H.; Currie, T.; García, L.; Jung, D.; Lintott, C.; McElwain, M.; Padgett, D. L.; Rebull, L. M.; Wisniewski, J. P.; Nesvold, E.; Schawinski, K.; Thaller, M. L.; Grady, C. A.; Biggs, J.; Bosch, M.; Černohous, T.; Luca, H. A. D.; Hyogo, M.; Wah, L. L. W.; Piipuu, A.; Piñeiro, F.; the Disk Detective Collaboration. DISK DETECTIVE: DISCOVERY OF NEW CIRCUMSTELLAR DISK CANDIDATES THROUGH CITIZEN SCIENCE. *ApJ* **2016**, 830 (2), 84. <https://doi.org/10.3847/0004-637X/830/2/84>.
22. Kumar, Y. B.; Reddy, B. E.; Lambert, D. L. ORIGIN OF LITHIUM ENRICHMENT IN K GIANTS. *ApJ* **2011**, 730 (1), L12. <https://doi.org/10.1088/2041-8205/730/1/L12>.

23. Li, X. et al. Distribution and Evolution of the Li Abundance in Red Clump Stars Can Be Explained by Internal Gravity Waves. *ApJ* 2023, 943 (2), 115. <https://doi.org/10.3847/1538-4357/acae9d>.
24. López-Valdivia, R. et al. Lithium Abundance in a Sample of Solar-like Stars. *Mon. Not. R. Astron. Soc.* 2015, 451 (4), 4368–4374. <https://doi.org/10.1093/mnras/stv1222>.
25. Lyubimkov, L. S.; Lambert, D. L.; Rostopchin, S. I.; Rachkovskaya, T. M.; Poklad, D. B. Accurate Fundamental Parameters for A-, F- and G-Type Supergiants in the Solar Neighbourhood. *Monthly Notices of the Royal Astronomical Society* **2010**, 402 (2), 1369–1379. <https://doi.org/10.1111/j.1365-2966.2009.15979.x>.
26. Marsteller, B. et al. AUTOMATED DETERMINATION OF [Fe/H] AND [C/Fe] FROM LOW-RESOLUTION SPECTROSCOPY. *The Astronomical Journal* 2009, 138 (2), 533–539. <https://doi.org/10.1088/0004-6256/138/2/533>.
27. Palacios, A. et al. The Lithium Flash: Thermal Instabilities Generated by Lithium Burning in RGB Stars. *A&A* 2001, 375 (1), L9–L13. <https://doi.org/10.1051/0004-6361:20010903>.
28. Rebull, L. M. et al. ON INFRARED EXCESSES ASSOCIATED WITH Li-RICH K GIANTS. *AJ*
29. Siess, L.; Livio, M. The Accretion of Brown Dwarfs and Planets by Giant Stars -- II. Solar-Mass Stars on the Red Giant Branch. *Monthly Notices of the Royal Astronomical Society* **1999**, 308 (4), 1133–1149. <https://doi.org/10.1046/j.1365-8711.1999.02784.x>.
30. Sun, W.; Duan, X.-W.; Deng, L.; De Grijs, R.; Zhang, B.; Liu, C. Exploring the Stellar Rotation of Early-Type Stars in the LAMOST Medium-Resolution Survey. I. Catalog. *ApJS* **2021**, 257 (2), 22. <https://doi.org/10.3847/1538-4365/ac1acf>.
31. Toonen, S.; Hamers, A.; Portegies Zwart, S. The Evolution of Hierarchical Triple Star-Systems. *Comput. Astrophys.* **2016**, 3 (1), 6. <https://doi.org/10.1186/s40668-016-0019-0>.
32. Wang, S. et al. The Optical to Mid-Infrared Extinction Law Based on the APOGEE, Gaia DR2, Pan-STARRS1, SDSS, APASS, 2MASS, and WISE Surveys. *ApJ* 2019, 877 (2), 116. <https://doi.org/10.3847/1538-4357/ab1c61>.
33. Wiese, W. L.; Fuhr, J. R. Accurate Atomic Transition Probabilities for Hydrogen, Helium, and Lithium. *Journal of Physical and Chemical Reference Data* **2009**, 38 (3), 565–720. <https://doi.org/10.1063/1.3077727>.

34. Zhang, X. et al. Population Synthesis of Helium White Dwarf–Red Giant Star Mergers and the Formation of Lithium-Rich Giants and Carbon Stars. *ApJ* 2020, 889 (1), 33. <https://doi.org/10.3847/1538-4357/ab5e89>.

Appendix A

Doppler Shift Calculation and Graphing Protocol

```
import numpy as np
import matplotlib.pyplot as plt
from astropy import units as u
from astropy.modeling import models, fitting
from specutils import Spectrum1D

# Load list of objects
filepaths = np.loadtxt('allspectrafiles.txt', dtype=str)
filepathsLinesCount = 0
with open('allspectrafiles.txt', "r") as f:
    lines = f.readlines()
    linesCount = len(lines)
    filepathsLinesCount = linesCount

# Define a spline model to fit the continuum (with least squares filter)
spline_model = models.Chebyshev1D(degree=200)

# Define the wavelength ranges for each subplot
wavelength_ranges = [
    (3920, 3980),
    (5150, 5190),
    (5870, 5930)
]

# Define a function to apply doppler shift
def apply_shift(spectral_axis, mean_doppler_shift):
    return spectral_axis / (1 + mean_doppler_shift)

# Define empty lists
all_shifts = []
all_statuses = []
all_std_shifts = []

# Lab standard rest wavelengths
reference_lines = {'Ca II 1': 3933.663 * u.AA, 'Ca II 2': 3968.469 * u.AA,
                  'Mg I': 5183.604 * u.AA, 'Na I': 5895.92 * u.AA}
reference_lines_filtered = {name: line for name, line in reference_lines.items()}

# Define doppler shift processing
def process_spectrum(file_path):
    wavarr, fluxread = np.loadtxt(file_path, unpack=True)

    # Fit the spline model to the data to estimate the continuum
    fitter = fitting.LinearLSQFitter()
    spline_fit = fitter(spline_model, wavarr, fluxread)

    # Calculate continuum by evaluating spline fit
    continuum = spline_fit(wavarr) - 1
```

```

# Normalize the spectrum by dividing by the continuum
norm_flux = fluxread / continuum

spectrum = Spectrum1D(spectral_axis=wavarr*u.AA, flux=norm_flux*u.Unit('erg cm-2 s-1 AA-1'))

# Calculate the nearest peaks for the reference lines in the spectrum
nearest_peaks = {}
for name, line in reference_lines_filtered.items():
    indices_within_range = np.where((spectrum.spectral_axis.value >= min(wavarr)) &
    (spectrum.spectral_axis.value <= max(wavarr)))[0]
    nearest_index =
    indices_within_range[np.argmin(np.abs(spectrum.spectral_axis[indices_within_range] - line))]
    nearest_peaks[name] = nearest_index

# Calculate the doppler shift for each reference line
doppler_shifts = {(name, peak): (spectrum.spectral_axis[peak].value - line.value) / line.value
    for (name, line), peak in zip(reference_lines_filtered.items(), nearest_peaks.values())}

print("{:<10} {:<15} {:<12} {:<15}".format("Peak Name", "Reference Line", "Nearest Peak", "Doppler
Shift"))
print("-" * 60)

for (name, peak), shift in doppler_shifts.items():
    nearest_peak_value = round(spectrum.spectral_axis[peak].value, 3)
    reference_line_value = round(reference_lines[name].value, 3)
    shift = round(shift, 7)
    print("{:<10} {:<15} {:<12} {:<15}".format(name, reference_line_value, nearest_peak_value,
    shift))

# Calculate the mean doppler shift
mean_doppler_shift = np.mean([shift for (name, shift) in doppler_shifts.items()])

# Calculate the mean doppler shifts' standard deviation
std_doppler_shift = np.std([shift for (name, shift) in doppler_shifts.items()])

if mean_doppler_shift < 0:
    print("Blue-shifted")
    shift_status = "blue-shifted"

else:
    print("Red-shifted")
    shift_status = "red-shifted"

# Apply doppler shift to the original spectrum
shifted_wavarr = apply_shift(spectrum.spectral_axis.value, mean_doppler_shift)
shifted_spectrum = Spectrum1D(spectral_axis=shifted_wavarr*u.AA, flux=norm_flux*u.Unit('erg cm-2
s-1 AA-1'))

return spectrum, shifted_spectrum, shifted_wavarr, mean_doppler_shift, shift_status, nearest_peaks,
std_doppler_shift

# Call doppler shift processing for all spectra
for file_path in filepaths:
    spectrum, shifted_spectrum, shifted_wavarr, mean_doppler_shift, shift_status, nearest_peaks,
    std_doppler_shift = process_spectrum(file_path)

```

```

# Create a new figure for each spectrum
fig, axs = plt.subplots(len(wavelength_ranges), 1, figsize=(10, 10))

# Iterate over each wavelength range and corresponding subplot
for i, (wav_min, wav_max) in enumerate(wavelength_ranges):
    ax = axs[i]

    # Filter observed spectrum within the current range
    mask = (spectrum.spectral_axis.value >= wav_min) & (spectrum.spectral_axis.value <=
wav_max)
    wav_range = spectrum.spectral_axis.value[mask]
    flux_range = spectrum.flux[mask]

    # Filter shifted spectrum within current range
    mask2 = (shifted_spectrum.spectral_axis.value >= wav_min) & (
shifted_spectrum.spectral_axis.value <= wav_max)
    shifted_wav_range = shifted_spectrum.spectral_axis.value[mask2]
    shifted_flux_range = shifted_spectrum.flux[mask2]

    # Plot original and doppler shifted spectra
    ax.plot(wav_range, flux_range, label=f'Original Spectrum ({wav_min}-{wav_max})',
color='blue')
    ax.plot(shifted_wav_range, shifted_flux_range, label='Doppler Shifted Spectrum',
color='orange')

    # Plot observed and reference lines within the wavelength range
    for ref_line_name, nearest_peak_index in nearest_peaks.items():
        if wav_min <= reference_lines[ref_line_name].value <= wav_max:
            # Plot observed peak as a vertical line
            ax.axvline(x=spectrum.spectral_axis[nearest_peak_index].value, color='gray',
linestyle='--')
            # Plot reference line as a vertical line
            ax.axvline(x=reference_lines[ref_line_name].value, color='gray', linestyle='-')

    # Plot all observed peak lines with specified colors
    for ref_line_name, nearest_peak_index in nearest_peaks.items():
        # Check if the reference line is within the specified wavelength range
        if ref_line_name in reference_lines_filtered:
            # X-coordinate of the observed peak
            ref_line_x = spectrum.spectral_axis[nearest_peak_index].value

            if ref_line_name.startswith('Ca II'):
                line_color = 'red'
            elif ref_line_name.startswith('Mg'):
                line_color = 'purple'
            elif ref_line_name.startswith('Na'):
                line_color = 'blue'
            obs_line_label = f'{ref_line_name} - Observed Peak'
            ax.axvline(x=ref_line_x, color=line_color, linestyle='--', label=obs_line_label)

    # Plot the rest wavelength lines
    if i == 0:
        for name, line in reference_lines_filtered.items():
            ax.axvline(x=line.value, color='gray', linestyle='--')

    ax.set_xlim(wav_min, wav_max)

```

```
ax.set_xlabel('Wavelength (Angstroms)')
ax.set_ylabel('Flux')
ax.legend(loc='center left', bbox_to_anchor=(1, 0.5))
ax.set_title(f'Comparison of Original and Doppler Shifted Spectra for {file_path}')
ax.grid(True)
```

```
plt.tight_layout()
plt.show()
```

Save the data to a text file

with open("spectra_dopplershift_status.txt", "w+") as file:

```
file.write("{:<25} {:<20} {:<20} {:<15}\n".format("File Path", "Mean Doppler Shift", "Std Dev Doppler Shift", "Shift Status"))
```

```
file.write("-" * 85 + "\n")
```

```
for file_path, shift, std_doppler_shift, status in zip(filepaths, all_shifts, all_std_shifts, all_statuses):
```

```
file.write("{:<25} {:<20} {:<20} {:<15}\n".format(file_path, round(shift, 9), round(std_doppler_shift, 9), status))
```

Appendix B

Manual Evaluation of Lithium Abundance via FGK LTE Gaia-ESO Curve of Growth

```
import numpy as np
from scipy.optimize import curve_fit
import matplotlib.pyplot as plt
import os
import re
import sys

file_path = 'Teff 5250 logg 2.5.txt'

with open(file_path, "r") as file:
    lines = file.readlines()[3:]

T_eff, log_g, Fe_H, A_Li, equivalence_width_LTE = np.loadtxt(lines, unpack=True)

# Create bounds for log_g and T_eff
log_g_bounds = (2.45, 2.55)
T_eff_bounds = (5245, 5255)

# Find indices of values within the bounds
indices = np.where((log_g >= log_g_bounds[0]) & (log_g <= log_g_bounds[1]) &
                  (T_eff >= T_eff_bounds[0]) & (T_eff <= T_eff_bounds[1]))

# Get the corresponding values for the other two variables
equivalence_width_LTE_within_bounds = equivalence_width_LTE[indices]
A_Li_within_bounds = A_Li[indices]

# Define quadratic function fit
def func(x, a, b, c):
    return a * x ** 2 + b * x + c

popt, pcov = curve_fit(func, A_Li_within_bounds, equivalence_width_LTE_within_bounds)

a_fit, b_fit, c_fit = popt

x_fit = np.linspace(2, 3, 100)
y_fit = func(x_fit, a_fit, b_fit, c_fit)

plt.plot(A_Li_within_bounds, equivalence_width_LTE_within_bounds, label = 'Gaia-ESO Survey Curve of Growth')
plt.plot(x_fit, y_fit, 'r-', label = 'Function Fit')
plt.xlabel('A(Li) (dex)')
plt.ylabel('Equivalence Width (mÅ)')
plt.legend(loc='best')
plt.title('Function Fit of Gaia-ESO FGK Curve of Growth', fontweight = 'bold')
plt.show()
```

```
# Define function to calculate A(Li) via Curve of Growth
def inverse_func(y, a, b, c):
    return np.roots([a, b, c - y])

# Input a y value (manual gaussian-fit EW) to find the corresponding x value
y_input = 519.426
x_corresponding = inverse_func(y_input, a_fit, b_fit, c_fit)

print("For EW =", y_input, "the corresponding A(Li) value is:", x_corresponding)
```

Appendix C

pyMOOG Metallicity Evaluation Using Chi-Squared Minimization Scheme

```
import numpy as np
import pandas as pd
import matplotlib.pyplot as plt
import pymoog
import os
import re
import sys
import astropy.units as u
from astropy.modeling import models, fitting
from scipy.optimize import minimize
from itertools import cycle
from tabulate import tabulate
import csv
import time
import os
from tabulate import tabulate
from scipy.interpolate import make_interp_spline

# Load list of doppler shifted spectra with corresponding teff and logg values
fast_spectra = np.loadtxt('FAST_teff_logg2.txt', dtype = str, skiprows=1)

# Determine number of lines in fast_spectra
fastSpectraLinesCount = 0
with open('FAST_teff_logg2.txt', "r") as f:
    lines = f.readlines()
    linesCount = len(lines)
    fastSpectraLinesCount = linesCount

# Load MARCS data
marcs_data = np.loadtxt('MARCS_teff_logg_metallicity.txt')

csv.field_size_limit(sys.maxsize) # Increase the maximum field size limit of csv file to handle large inputs
csv_file_path = "cache.csv"
cache = {}

# Define a spline model to fit the continuum (with least squares filter)
spline_model = models.Chebyshev1D(degree = 200)

# Define resolution
resolution = 1200

mc_plots_directory = "Chi2_vs_Metallicity_Plots"
spectra_plots_directory = "observed_synthetic_bestchi2range"

def calculate_chi2(synthetic, observed):
    chi2 = np.sum(((synthetic - observed) ** 2)/observed)
    return chi2
```

```

def write_to_csv(key, synth_wav, synth_flux):
    with open(csv_file_path, mode='a', newline='') as f:
        writer = csv.writer(f, delimiter=',')
        writer.writerow([key, ','.join(map(str, synth_wav)), ','.join(map(str, synth_flux))])

def process_spectrum(file_path, Teff,logg, i, wav_min, wav_max):
    print("status: ", f"{round((i + 1) / fastSpectraLinesCount, 5) * 100}%")

    wavarr, fluxread = np.loadtxt(file_path, unpack=True)

    # Fit the spline model to the data to estimate the continuum
    fitter = fitting.LinearLSQFitter()
    spline_fit = fitter(spline_model, wavarr, fluxread)

    # Calculate the continuum by evaluating the spline fit
    continuum = spline_fit(wavarr)

    # Normalize the spectrum by dividing by the continuum
    norm_flux = fluxread / continuum

    # Load observed spectrum
    observed_wav = np.array(wavarr)
    observed_flux = np.array(norm_flux)

    # Indices corresponding to desired wavelength range
    wav_indices = np.where((observed_wav >= wav_min) & (observed_wav <= wav_max))[0]
    observed_wav_range = observed_wav[wav_indices]
    observed_flux_range = observed_flux[wav_indices]

    # Trim observed arrays to ensure consistent length
    min_length = min(len(observed_wav_range), len(observed_flux_range))
    observed_wav_range = observed_wav_range[:min_length]
    observed_flux_range = observed_flux_range[:min_length]

    # Find closest teff and logg values in the dataset
    closest_teff = marcs_data[:,0][np.argmin(np.abs(marcs_data[:,0] - Teff))]
    closest_logg = marcs_data[:,1][np.argmin(np.abs(marcs_data[:,1] - logg))]

    # Filter data to get available metallicity for teff & logg
    mask = (marcs_data[:,0] == closest_teff) & (marcs_data[:,1] == closest_logg)
    available_metallicities = marcs_data[mask][:,2]

    # Sort available unique metallicities in ascending order
    marcs_metallicities = np.sort(np.unique(available_metallicities))
    marcs_metallicities = marcs_metallicities[(marcs_metallicities >= -2)&(marcs_metallicities <= 2)]

    # Initialize variables
    best_chi2 = np.inf
    best_metallicity = None

    # Define empty lists to store best results
    best_chi2_values = []
    best_metallicity_values = []
    metallicities = []
    chi2_values = []

```

```

# Loop over different metallicities
for metallicity in marcs_metallicities:
    synth_wav = None
    synth_flux = None
    key = f"{closest_teff} {closest_logg} {metallicity} {wav_min} {wav_max} {resolution}"
    # Note: key = (closest_teff, closest_logg, metallicity, wav_min, wav_max, resolution)
    if key in cache:
        synth_wav = cache[key][0]
        synth_flux = cache[key][1]
    else:
        # Generate synthetic spectra
        s = pymoog.synth.synth(closest_teff, closest_logg, metallicity, wav_min, wav_max,
                               resolution)
        s.prepare_file()
        s.run_moog()
        s.read_spectra()

        synth_wav = np.array(s.wav)
        synth_flux = np.array(s.flux)

        # Write to cache
        write_to_csv(key, synth_wav.tolist(), synth_flux.tolist())

        # Check if the CSV file exists
        file_exists = os.path.isfile(csv_file_path)
        write_to_csv(key, synth_wav.tolist(), synth_flux.tolist())

        # Normalize the synthesized spectra to have a mean value of 1
        mean_flux = np.mean(synth_flux)
        norm_synth_flux = synth_flux / mean_flux

        # Interpolate generated synthetic spectrum
        interpolated_synth_flux = np.interp(observed_wav_range, synth_wav, norm_synth_flux)

        # Calculate chi-squared for synthetic spectrum
        chi2 = calculate_chi2(interpolated_synth_flux, observed_flux_range)

        metallicities.append(metallicity)
        chi2_values.append(chi2)

        if chi2 < best_chi2:
            best_chi2 = chi2
            best_metallicity = metallicity

        plt.scatter(metallicities, chi2_values, marker = 'o')
        plt.plot(metallicities, chi2_values, color = 'red', linestyle = '-', linewidth = 0.5, label = f'Wavelength
        Range {j+1}')

    return best_metallicity, best_chi2, observed_wav_range, observed_flux_range,
    interpolated_synth_flux, (wav_min, wav_max), metallicities, chi2_values

results = []

row_index = 0

```

```

# Define wavelength ranges
wavelength_ranges = [
    (5000, 5500),
    (5500, 6000),
    (6000, 6500)
]

for i, row in enumerate(fast_spectra):
    file_path, Teff, logg = row
    Teff = float(Teff)
    logg = float(logg)
    plt.figure(figsize=(10, 6))

    # Initialize table_data
    table_data = [
        ["Wavelength Range", "Best Metallicity", "Best Chi2"]
    ]

    # Initialize lists to store all metallicities and chi2 values for all wavelength ranges
    all_metallicities = []
    all_chi2_values = []

    for j, wav_range in enumerate(wavelength_ranges):
        mask = (np.array(all_metallicities) >= wav_range[0]) & (np.array(all_metallicities) <=
            wav_range[1])

        best_metallicity, best_chi2, observed_wav_range, observed_flux_range, interpolated_synth_flux,
        (wav_min, wav_max), metallicities, chi2_values = process_spectrum(file_path, Teff, logg, i, wav_range[0],
            wav_range[1])

        # Add data to table
        table_data.append([wav_range, best_metallicity, best_chi2])

        # Store metallicities and chi2 values
        all_metallicities.extend(metallicities)
        all_chi2_values.extend(chi2_values)

        # Find the optimal metallicity (associated with the lowest chi-squared value)
        optimal_index = all_chi2_values.index(min(all_chi2_values))
        optimal_metallicity = all_metallicities[optimal_index]
        optimal_chi2 = min(all_chi2_values)

        # Highlight the point with optimal metallicity
        plt.scatter(optimal_metallicity, optimal_chi2, color='blue', label=f'Optimal Metallicity
            ({optimal_metallicity}, {optimal_chi2:.2f})')

    plt.xlabel('Metallicity [Fe/H]')
    plt.ylabel('Chi-Squared Value')
    plt.title(f'Chi-squared Values vs. Metallicities for {file_path}')
    plt.legend()
    plt.grid(True)
    plot_filename = f'chi2_metallicity_plot_{os.path.basename(file_path)}.png'
    plt.savefig(os.path.join(mc_plots_directory, plot_filename))
    plt.show()

```

```
# Add data to results
results.append({
    'file_path': file_path,
    'Teff': Teff,
    'logg': logg,
    'best_metallicity': optimal_metallicity,
    'best_chi2': optimal_chi2
})

# Print table data
print(tabulate(table_data, headers="firstrow"))
print()

# Print results
for result in results:
    print(result)
```

Appendix D

Neutral Iron Lines' Identification, FWHM Calculation, and Projected Rotational Velocity Specutils Protocol

```
import numpy as np
import pandas as pd
import matplotlib.pyplot as plt
import pymoog
import os
import re
import sys
import csv
import time
from astropy.modeling import fitting
from astropy.modeling.models import Chebyshev1D

import astropy.units as u
from astropy.modeling import models, fitting
from astropy.nddata import StdDevUncertainty
from astropy.utils.exceptions import AstropyUserWarning
from astropy.utils.exceptions import AstropyWarning
from scipy.optimize import minimize
from itertools import cycle
from tabulate import tabulate

from specutils import Spectrum1D, analysis
from specutils import SpectralRegion
from specutils.fitting import fit_lines
from specutils.fitting import fit_generic_continuum
from specutils.analysis import snr, equivalent_width, centroid, gaussian_sigma_width

# IRON LINES IDENTIFICATION

# Define the spline model for continuum fitting
spline_model = Chebyshev1D(degree=200)

# Read lines from the file
input_file = "FAST_teff_logg_metallicity_redshift.txt"
with open(input_file, 'r') as file:
    lines = file.readlines()

# Initialize an empty list to store the data
data = []

# Iterate over lines, splitting and converting values
for line in lines:
    values = line.strip().split()
    if len(values) >= 4:
        file_path, Teff, logg, metallicity = values[:4]
        redshift = values[4] if len(values) > 4 else None
```

```

# Check if each value is a valid float
try:
    # Convert '-' to a negative float if necessary
    Teff = float(Teff) if Teff != '-' else -float(Teff[1:])
    logg = float(logg) if logg != '-' else -float(logg[1:])
    metallicity = float(metallicity) if metallicity != '-' else -float(metallicity[1:])
    redshift = float(redshift) if redshift is not None and redshift != '-' else 0.0
except ValueError:
    # Handle the case where a value couldn't be converted to float
    print(f"Skipping line due to invalid float value: {line}")
    continue

data.append([file_path, Teff, logg, metallicity, redshift])
else:
    print(f"Skipping line: {line}")

# Define the wavelength ranges for each subplot
wavelength_ranges = [
    (5850, 6000),
    (6100, 6300),
    (6500, 6600)
]

# Iterate over each spectrum file
for row in data:
    file_path = row[0]
    Teff = row[1]
    logg = row[2]
    metallicity = row[3]
    redshift = row[4]

    # Load spectrum data
    wavarr, fluxread = np.loadtxt(file_path, unpack=True)

    # Fit continuum to the spectrum
    fitter = fitting.LinearLSQFitter()
    spline_fit = fitter(spline_model, wavarr, fluxread)
    continuum = spline_fit(wavarr)

    # Normalize the spectrum by dividing by the continuum
    norm_flux = fluxread / continuum

    # Create a new figure for each spectrum
    fig, axs = plt.subplots(3, 1, figsize=(10, 10))

    # Iterate over each wavelength range and corresponding subplot
    for i, (wav_min, wav_max) in enumerate(wavelength_ranges):
        ax = axs[i] # Select the subplot

        # Filter wavelength and flux within the current range
        mask = (wavarr >= wav_min) & (wavarr <= wav_max)
        wav_range = wavarr[mask]
        flux_range = norm_flux[mask]

        # Plot the spectrum in the current subplot
        ax.plot(wav_range, flux_range, label=file_path)

```

```

ax.set_xlabel('Wavelength (Angstroms)')
ax.set_ylabel('Flux')

# Add vertical lines for Fe I lines
fe_lines = [5916.25, 6188.00, 6240.65, 6574.23]
for fe_line in fe_lines:
    if wav_min <= fe_line <= wav_max:
        ax.axvline(fe_line, color='red', linestyle='--', label=f'Fe I ({fe_line})')

# Add legend for the subplot
ax.legend()

# Adjust layout
fig.tight_layout()
fig.subplots_adjust(top=0.92)

# Show the plot
plt.show()

# FWHM & PROJECTED ROTATIONAL VELOCITY CALCULATION

input_file = "FAST_teff_logg_metallicity_redshift.txt"

# Read lines from the file
with open(input_file, 'r') as file:
    lines = file.readlines()

# Initialize an empty list to store the data
data = []

# Iterate over lines, splitting and converting values
for line in lines:
    values = line.strip().split()
    if len(values) >= 4:
        file_path, Teff, logg, metallicity, *redshift = values
        data.append([file_path, float(Teff), float(logg), float(metallicity), float(redshift[0]) if redshift else
        None])
    else:
        print(f"Skipping line: {line}")

# Convert the list of lists to a NumPy array
fast_spectra = np.array(data)

# Iron wavelengths
wavelengths = [5916.25, 6188.0, 6240.65, 6574.23]

# Error from instrumental broadening
instrumental_broadening = 6 * u.angstrom

# Define the speed of light
c = 299792.458 * u.km / u.s

vsini_values = []

for row in fast_spectra:
    file_path = row[0]

```

```

wavarr, fluxread = np.loadtxt(file_path, unpack=True)
corrected_wavarr = wavarr - row[-1] if row[-1] is not None else wavarr

vsini_row = [file_path]

vsini_values_per_path = []
fwhm_values_per_path = []

print(f'file path:', file_path)
print(f'wavarr, fluxread:', wavarr, fluxread)

# Iterate over each iron line wavelength
for wavelength in wavelengths:
    # Find the index of the wavelength closest to the desired wavelength
    index = np.argmin(np.abs(corrected_wavarr - wavelength))

    # Extract a small window around the desired wavelength for fitting
    window_width = 10.0
    window = (corrected_wavarr >= wavelength - window_width / 2) & (corrected_wavarr
    <= wavelength + window_width / 2)
    wav_window = corrected_wavarr[window]
    flux_window = fluxread[window]

    flux_window = flux_window * u.Jy
    wav_window = wav_window * u.angstrom

    # Convert the flux and wavelength arrays to a Spectrum1D object
    spectrum = Spectrum1D(flux=flux_window, spectral_axis=wav_window)

    # Assume fwhm_value is in Angstroms
    fwhm_value = fwhm(spectrum)
    print(f'FWHM:', fwhm_value)

    # Convert the spectral line wavelength to Angstroms (if not already)
    lambda0 = wavelength * u.angstrom
    print(f'lambda0:', lambda0)

    # Compute projected rotational velocity ( $v \cdot \sin(i)$ )
    numerator = np.sqrt((fwhm_value*u.angstrom**2)-(instrumental_broadening**2))

    denominator = lambda0

    v_sin_i = (numerator / denominator) * (c / 2)

    vsini_row.append(v_sin_i)
    vsini_values_per_path.append(v_sin_i.value)
    fwhm_values_per_path.append(fwhm_value.value)

# Calculate average vsini for this file path
avg_vsini = np.mean(vsini_values_per_path)

# Calculate average FWHM for this file path
avg_fwhm = np.mean(fwhm_values_per_path)

# Append average vsini and FWHM to the row
vsini_row.extend([avg_fwhm, avg_vsini])

```

```

# Append the vsini row to the vsini values list
vsini_values.append(vsini_row)

# Convert vsini values to a NumPy array
vsini_array = np.array(vsini_values)

# Print results table with file paths
print("Filepath | Avg_FWHM | Avg_vsini |")
print("=====+=====+=====+")
for row in vsini_array:
    print("| {:<10} | {:<10.5f} | {:<10.5f} |".format(row[0], float(row[-2]), float(row[-1])))
    print("+-----+-----+-----+")

```